Received: 17 May 2021 | Revised: 13 August 2021 | Accepted: 18 August 2021

DOI: 10.1002/esp.5233

RESEARCH ARTICLE

ESPL WILEY

The role of bathymetry and directional wave conditions on observed crescentic bar dynamics

Rinse L. de Swart[1] | Francesca Ribas[1] | Gonzalo Simarro[2] | Jorge Guillén[2] | Daniel Calvete[1]

[1]Department of Physics, Universitat Politècnica de Catalunya (UPC), Barcelona, Spain

[2]Department of Marine Geosciences, Institut de Ciències del Mar (ICM-CSIC), Barcelona, Spain

Correspondence
Rinse L. de Swart, Department of Physics, Universitat Politècnica de Catalunya (UPC), Jordi Girona, 1–3, 08034, Barcelona, Spain.
Email: rinse.de.swart@upc.edu

Funding information
Spanish government, Grant/Award Numbers: CTM2015-66225-C2-1-P, CTM2015-66225-C2-2-P, RTI2018-093941-B-C32, RTI2018-093941-B-C33

Abstract

Nearshore sandbars are important features in the surf zone of many beaches because they strongly influence the mean circulation and evolving morphology. Due to variations in wave conditions, sandbars can experience cross-shore migration and vary in shape from alongshore uniform (shore-parallel) to alongshore rhythmic (crescentic). Sandbar dynamics have been studied extensively, but existing observational studies usually do not quantify the processes leading to crescentic bar formation and straightening. This study analyses the dynamics of crescentic bar events at the fetch-limited beach of Castelldefels (northwestern Mediterranean Sea, Spain) using 7.5 years of hourly time-exposure video images and detailed wave conditions. The results show that, despite the generally calm wave conditions, the sandbars were very dynamic in the cross-shore and longshore directions. They often migrated rapidly offshore during storms (up to 70 m in one day) and more slowly onshore during post-storm conditions. Crescentic bars were often present at the study site (48% of the time), but only when the sandbar was at least 10 m from the shoreline. They displayed a large variability in wavelengths (100–700 m), alongshore migration speeds (0–50 m/day) and cross-shore amplitudes (5–20 m). Wavelengths increased for larger bar–shoreline distances and the alongshore migration speeds were strongly correlated with the alongshore component of the radiation stresses. Crescentic patterns typically developed during low–medium energetic waves with limited obliquity ($\theta \lesssim 20^\circ$ at 10 m depth), while bar straightening occurred during medium–high energetic waves with strong oblique angles of incidence ($\theta \gtrsim 15^\circ$). Overall, this study provides further proof for the important role of wave direction in crescentic bar dynamics and highlights the strong dependence of crescentic bar development on the initial bathymetric configuration.

KEYWORDS
beach morphology, Mediterranean Sea, nearshore sandbars, oblique waves, rip-channel systems, video monitoring

1 | INTRODUCTION

The nearshore zone of sandy dissipative beaches commonly features one or more shallow submerged sandbars. These sandbars are typically dynamic and display a variety of complex morphological patterns in response to variations in hydrodynamics and sediment transport. Two common patterns are shore-parallel and crescentic sandbars (sometimes called rip-channel systems), the latter consisting of an alongshore rhythmic pattern of undulations with shoreward horns (shallow areas) and seaward bays (deeper regions; e.g., Ribas et al.,

2015; Van Enckevort et al., 2004; and references therein). The evolution of nearshore sandbars is of interest for coastal management as they induce wave breaking and influence sediment transport patterns, but also because morphological coupling between sandbar and beach/shoreline (e.g., Orzech et al., 2011; Van de Lageweg et al., 2013) can lead to changes in beach width and alongshore variability in dune erosion (Castelle et al., 2015; Thornton et al., 2007). Furthermore, the rip currents that accompany crescentic bars are relevant for ecology (redistribution and offshore transport of nutrients and biota), cross-shore mixing of particles (sediments or pollutants) and also pose a significant safety risk for swimmers (e.g., Castelle & Coco, 2013; Castelle et al., 2016).

Sandbar variability has attracted the attention of nearshore scientists for decades. The development of a method to track the location of sandbars based on the wave-breaking pattern in time-exposure video images (Holman & Stanley, 2007; Lippmann & Holman, 1989) resulted in a large number of studies investigating their dynamics (e.g., Bouvier et al., 2017; Lippmann & Holman, 1990; Price & Ruessink, 2011; Rutten et al., 2018; Van Enckevort et al., 2004), while other studies continued using long-term bathymetric datasets (e.g., Aleman et al., 2015; Arifin & Kennedy, 2011; Castelle et al., 2007; Gijsman et al., 2021). This resulted in relatively good knowledge regarding the processes behind onshore and offshore sandbar migration (e.g., Aleman et al., 2017; Gallagher et al., 1998; Ruessink et al., 2009), and the discovery of monthly–annual sandbar cycles of formation near the shore, net offshore migration and seaward degeneration (NOM pattern; Ruessink & Kroon, 1994; Shand et al., 1999). The alongshore variability of sandbars was investigated by many other studies (e.g., Almar et al., 2010; Price & Ruessink, 2011; Van Enckevort et al., 2004; Wright & Short, 1984), which generally observed crescentic bars to develop during post-storm wave conditions with angles close to shore-normal and to disappear during higher energetic wave conditions (e.g., Wright & Short, 1984) or more oblique angles of incidence driving a strong alongshore current (Contardo & Symonds, 2015; Price & Ruessink, 2011). The different stages of the sandbar evolution at weekly time scales were summarized in a widely accepted beach state classification scheme (Lippmann & Holman, 1990; Wright & Short, 1984), which was later extended to double-barred beaches (Price & Ruessink, 2011; Short & Aagaard, 1993). Previous studies also found a large variety in crescentic bar characteristics, with average wavelengths varying from 100 m to several kilometres and average cross-shore amplitudes (defined as half the cross-shore distance between successive horns and bays) varying from 5 to 50 m (e.g., Arifin & Kennedy, 2011; Athanasiou et al., 2018; Van Enckevort et al., 2004). Furthermore, crescentic bar patterns were found to migrate alongshore at rates up to 100 m/day, presumably due to strong alongshore currents (Holman et al., 2006; Orzech et al., 2010; Ruessink et al., 2000; Van Enckevort et al., 2004).

Crescentic bars were also studied extensively using morphodynamic models, which were able to successfully reproduce some of the characteristics of crescentic bars observed in the field. For example, crescentic bar formation for shore-normal waves (e.g., Calvete et al., 2005; Castelle & Ruessink, 2011; Deigaard et al., 1999; Garnier et al., 2008; Reniers et al., 2004; Smit et al., 2008) as well as bar straightening during obliquely incident waves (Garnier et al., 2013) were successfully simulated. Models also predict that crescentic bar formation is strongly related to the underlying bathymetry (Calvete et al., 2007; Smit et al., 2012; Tiessen et al., 2011). However, model predictions are not always in line with field observations, and model validation is in general difficult due to lack of suitable field data.

The roles of wave direction and bathymetric configuration in crescentic bar formation/straightening are not yet clear, mainly because the available observational studies do not usually quantify the formation/straightening moments. Apart from that, existing observational studies on crescentic bars are often limited in duration (e.g., Van Enckevort et al., 2004) or temporal resolution (e.g., Athanasiou et al., 2018). Moreover, they generally focus on beaches that are either characterized by substantial tidal range (> 1 m) and highly energetic (H_{m0} > 1 m) waves (Holman et al., 2006; Price & Ruessink, 2011; Van Enckevort et al., 2004) or a long fetch (e.g., Contardo & Symonds, 2015). Furthermore, crescentic bar studies in low-energetic environments with almost no tides and small fetches (such as the Mediterranean Sea) are scarce. Mediterranean studies include Israel (Goldsmith et al., 1982), Italy (Armaroli & Ciavola, 2011; Parlagreco et al., 2019), Spain (Ojeda et al., 2011) and France (Bouvier et al., 2017; Gervais et al., 2012), with Ribas et al. (2017) providing an overview of sandbar studies in the Western Mediterranean. Unfortunately, most of these studies examine relatively short time spans and do not study the crescentic bar dynamics in detail.

The main objective of the present study is to quantify the role of directional wave conditions and the bathymetric configuration on crescentic bar development and straightening. This will be done using a dataset of nearly 8 years of hourly video images and optimal hourly wave conditions at the open, low-energetic, tideless beach of Castelldefels (northwestern Mediterranean Sea, Catalunya, Spain). First, the study site, dataset and analysis methods are described. Subsequently, the results of quantifying the crescentic bar events and correlating them with the wave and morphological conditions are presented, paying special attention to the formation and straightening moments. The main findings of this study are compared in the discussion with previous observations and model studies. Lastly, the most important outcomes are listed in the conclusions.

2 | STUDY AREA AND DATA COLLECTION

2.1 | Study site

Castelldefels beach is located approximately 20 km southwest of Barcelona, at the Spanish Catalan coast (northwestern Mediterranean Sea; Figure 1). It is an open, double-barred beach located in the middle of the Llobregat Delta, formed by a continuous stretch of beaches that extend over an alongshore distance of 18 km. The study site is a 1 km beach section with an east–west alignment (89° with respect to north). Castelldefels beach is mainly composed of sand with a median grain size of 270 μm, and the nearshore bed slope is approximately 0.014 (Figure 2). The tide in this part of the Mediterranean Sea is negligible, with a tidal range of approximately 20 (10) cm during spring (neap) tide, so that it is considered a tideless beach (Simarro et al. 2015).

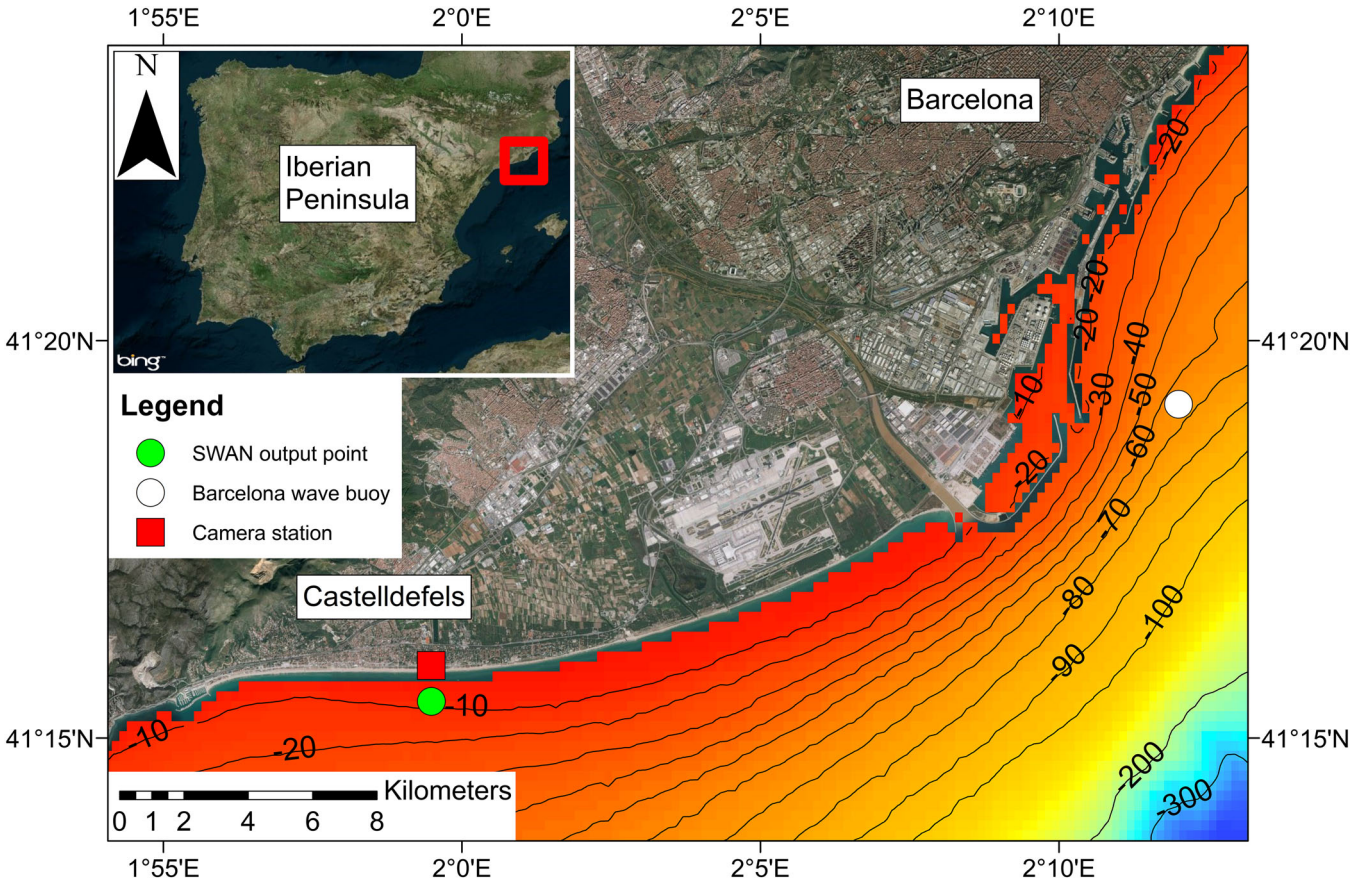

FIGURE 1 Overview map showing the study site, the nearshore bathymetry (source Emodnet) and the locations of the Barcelona wave buoy and the SWAN output point. The aerial photography is part of Microsoft Bing Maps (© 2019 Microsoft Corporation Earthstar Geographics SIO)

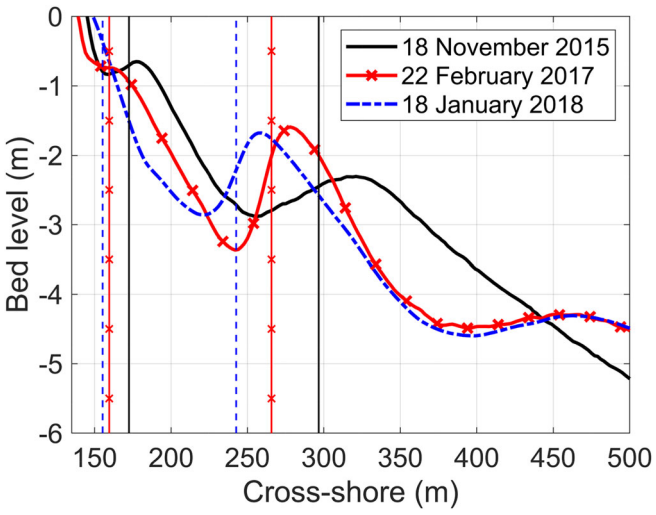

FIGURE 2 Measured alongshore-averaged cross-shore profiles at Castelldefels beach on 18 November 2015 (inner bar), 22 February 2017 (inner terrace) and 18 January 2018 (no inner bar/terrace). The vertical lines indicate the alongshore-averaged barline positions derived from the time-exposure images closest to the bathymetry dates

Castelldefels is exposed to waves throughout the year. The long-term average values during the entire study period (October 2010 to August 2018) of the significant wave height H_{m0} and mean zero-crossing period T_{m02} at the Barcelona wave buoy (68 m depth) are 0.73 m and 3.8 s, respectively. Waves generally come from two dominant directions (east-southeast and south-southwest; De Swart et al., 2020) with average mean wave directions θ_{mean} of 100° and 176° (with respect to north), respectively. The wave climate is generally characterized by calm wave conditions with occasional high-energetic wave events ($H_{m0} > 1.5$ m at deep water Puertos del Estado, 1994). Storm conditions along the Catalan coast are generally short lived because of the limited fetches, with an average storm duration of less than 24 h. Above-average wave heights are predominantly observed between September and March. Due to the longest available fetches, the largest storms in this part of the Catalan coast come from the east (Bolaños et al., 2009; Sánchez-Arcilla et al., 2008).

2.2 | Morphological data

During spring 2010, a video monitoring system was installed at Castelldefels beach at the top of a 30 m high observation tower. The system consists of five full-colour cameras that cover a 180° overview of the shoreline. The system uses the Sirena open source code (Nieto et al., 2010) and operates since 5 October 2010. Each daylight hour, all the cameras produce one snapshot, one time exposure and one variance image. The time exposure images are obtained by averaging numerous instantaneous snapshots during a 10 min period. The images of the five cameras are georeferenced, rectified and merged into a planview using the Ulises software (Simarro et al., 2017). The conversion from image to real-world coordinates is done by linking a

set of clearly visible ground control points with known real-world coordinates to their image coordinates. The resulting planviews (Figure 3) span 1000 m in the alongshore and 300 m in the cross-shore direction, and the pixel resolution is 0.5 m. The origin of the coordinate system (WGS84) in the planviews is the location of the camera system (41°15'54.7"N, 1°59'29.1"E).

The study period spans from 5 October 2010 to 31 August 2018 (2888 days). On some occasions, the planviews did not cover the complete study area due to partial camera failure. These cases were only included in the analysis when at least two adjacent cameras were functioning. Furthermore, there were periods without any images, the longest being from 27 September 2016 to 30 January 2017 (126 days), due to a renovation of the camera system. During the remainder of the study period (2762 days) there were only 98 days without any images (due to camera malfunction or insufficient image quality). The time-exposure images show the areas of dominant wave breaking as clear white stripes (Figure 3), which is a good proxy for the location of submerged sandbars (e.g., Holman & Stanley, 2007). As a result, the number of images suited for analysis was further limited by insufficient wave breaking over the bars. Fortunately, this is an indication of low-energetic wave conditions, meaning that no major morphological changes will occur.

The camera images are complemented by a total of nine topo-bathymetric surveys that were obtained irregularly during the study period and comprise the dry beach and the nearshore bathymetry up to a depth of 20 m (1700 m offshore). All surveys show a clear outer bar (between 100 and 200 m from the shoreline at a depth of 1.5–2.5 m), and the majority of the surveys indicate the presence of an inner bar or terrace (between 0 and 50 m from the shoreline at a depth of 0.5–1.5 m). Unfortunately, six of the surveys lack data in the inner surf zone (depth between 0.5 and 1.5 m), preventing us from distinguishing between an inner bar, an inner terrace or no inner bar/terrace. Figure 2 shows three examples of alongshore-averaged cross-shore profiles at Castelldefels beach obtained from the three complete bathymetries.

2.3 | Wave data

Hourly wave conditions were obtained from the Barcelona wave buoy (data available 97% of the time), located at 68 m depth in front of Barcelona harbour (Figure 1). The buoy provides full 2D frequency–direction spectra as well as integrated wave parameters (such as H_{m0}, T_{m02} and θ_{mean}). The measured wave conditions were propagated to 10 m depth in front of the study site using SWAN (De Swart et al., 2020). The SWAN output data include integrated wave parameters as well as the 2D frequency–direction spectra. Two types of SWAN simulations were done: one used the measured 2D spectra as offshore boundary conditions, while the other was forced with the measured integrated wave parameters. Since forcing SWAN with 2D spectra yields the best results at the point of interest (particularly regarding θ_{mean} and the 2D spectra), the simulation forced with integrated wave parameters is only used sporadically (with illustrative purposes) to complement the simulation forced with 2D spectra at the moments when the latter were not available (2.8% of the time). More details regarding the wave propagation and an extensive validation of different propagation methods can be found in De Swart et al., (2020).

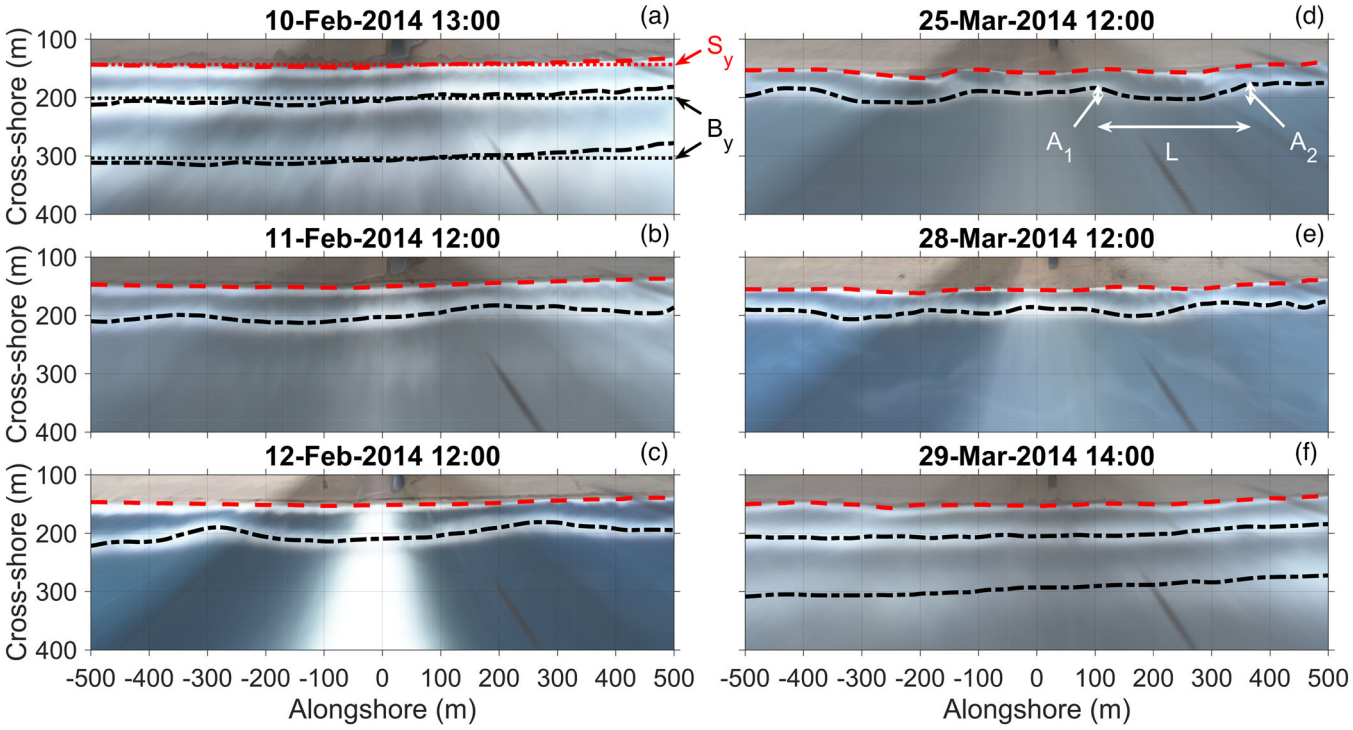

FIGURE 3 Planview images of Castelldefels beach showing the formation (a–c), development (d) and straightening (e,f) of a crescentic bar event. The tracked barlines $B(y)$ and shorelines $S(y)$ are plotted in all planviews. Furthermore, (a) also shows the alongshore-averaged bar- and shoreline positions B_y and S_y, whereas (c) shows an example of sun glare in the planview and (d) shows examples of wavelength L and the amplitudes A_1 and A_2. The amplitude A is defined as $A = \frac{1}{2}\left(\frac{A_1+A_2}{2}\right)$

3 | METHODS

3.1 | Visual analysis and data collection

A visual analysis of daily planview images (at 12:00 midday) was first carried out separately by two experienced researchers in order to reduce subjectivity. The occurrence of crescentic bar events in the sandbars was tracked, including dates of formation and straightening. Subsequently, both analyses were compared and the inconsistencies in crescentic bar presence (only 4% of the time) were cross-checked in order to increase accuracy and obtain the final visual analysis. Normally, a crescentic bar event was defined when at least three clear undulations with a certain rhythmicity occupied at least half of the planview images for at least 2 days. Crescentic patterns with two undulations were also considered if the wavelength was too large for more undulations to fit in the planview domain. One-day events were considered in case a clear rhythmic pattern occurred in the entire planview domain. An event was assumed to continue during an image gap when the crescentic bar pattern in the first image after the gap was similar to that in the last image before the gap. Special attention was paid to detecting the formation and straightening moments of the crescentic bar events (Figure 3). A formation moment (Figure 3b) was defined as the first day where, following a period with alongshore-uniformity, a crescentic pattern occurred in the planview images. Planview images in which the bar rhythmicity was strengthened (e.g., a clear increase in amplitude) were classified as reinforcement moments and included in the dataset with formation moments. A straightening moment (Figure 3f) was the first day where, following a period with crescentic bars, the bar was again alongshore uniform. Planview images in which the bar rhythmicity was weakened (e.g., a clear decrease in amplitude) but the crescentic pattern persisted (same rip locations, identical wavelengths) were classified as partial straightening moments and included in the dataset with straightening moments. A separation was made between unclear formation/straightening moments (e.g., no images available) and clear formation/straightening moments.

Hourly shorelines were extracted from all planview images using the uShore software (Ribas et al., 2020). This methodology combines the shorelines detected with four standard procedures to produce an accurate shoreline, with cross-shore errors below 2.5 m at this site. The default settings recommended in Ribas et al. (2020) were used, except for those related with the space–time filtering of the final shoreline. Here, no time filtering was applied and a 20 m window was used for the moving average in space. Subsequently, a visual evaluation of the shorelines was conducted to pick the best shoreline per day. For the 145 days on which the uShore software did not provide a shoreline of sufficient quality, the shoreline was manually digitized using the best-quality planview image. In total, shorelines were obtained for all days with camera images (2664 images in total; see examples in Figure 3).

The BarLine Intensity Mapper (BLIM; Pape, 2008) was used to track the breaker lines (from now on called barlines) in the planview images. This algorithm (Van Enckevort & Ruessink, 2001) detects the cross-shore location of the maximum breaker intensity value for each alongshore location. However, the barlines obtained from BLIM and the real bar crest locations are normally not identical, due to changes in water level, offshore wave height and the underlying sandbar geometry (Ribas et al., 2010; Van Enckevort & Ruessink, 2001). At the study site, the cross-shore distance between real and videoed alongshore-averaged barlines for the outer bar (using the nine topo-bathymetric surveys) was on average 16 m, with the videoed barlines located shoreward of the real barlines (see examples in Figure 2). Comparable results were obtained at two nearby single-barred beaches by Ribas et al. (2010). For the inner bar, the difference between real and videoed alongshore-averaged barlines (computed for the only two topo-bathymetric surveys with measured inner bar or terrace) was much smaller (5 and 6 m, respectively; Figure 2), presumably because the outer bar filters out the larger waves before they reach the inner bar (tidal action is negligible at the study site). Prior to tracking the barlines, a visual quality assessment of all planview images was performed to select, for each day, the image with better quality (foam presence, minimum sun glare, good contrast). Generally, the images around midday were selected because the sun is highest in the sky (minimizing sun glare). One image per day was usually enough for tracking the barlines, but up to three images per day were used when fast changes in the wave breaking pattern occurred within one day. Days without a clear wave-breaking pattern in the images or that only contained low-quality images were removed from the analysis. In total, barlines were extracted from 2279 images (2208 days) using BLIM (see examples in Figure 3).

3.2 | Bar and shoreline characterization

For each BLIM image, the cross-shore bar crest positions B at time t and alongshore position y were stored in a matrix $B(t, y)$ and the corresponding shoreline positions S were stored in a matrix denoted $S(t, y)$. Time series of the alongshore-averaged bar crest positions $B_y(t)$ and alongshore-averaged shoreline positions $S_y(t)$ were also obtained (Figure 3a). The alongshore-averaged distance between the sandbars and shorelines $D_y(t)$ was computed by subtracting S_y from B_y. Finally, the sinuosity $Sin_B(t)$ of the bar crest positions was also computed (total bar length divided by the distance between first and last point; Ojeda et al., 2011). In the barlines corresponding to a crescentic bar, all bays and horns were detected under the conditions that the cross-shore distance between a successive bay and horn was at least 6 m and the alongshore distance did not exceed 500 m. These constraints were enforced to prevent the detection of small (typically short-lived) wobbles as crescentic bars and to ensure that at least one complete undulation (consisting of two horns and one bay) was present in the planview domain. Following Van Enckevort et al. (2004), the wavelength L was computed for each undulation as the alongshore distance between the horns and the amplitude A was computed as half the average cross-shore distance between the bay and the two adjacent horns (Figure 3d). Within the same barline, the variation in A was mostly small (average standard deviation of 2 m), while L typically showed more variation (average standard deviation of 65 m). For each barline, L and A were averaged over all undulations to obtain the alongshore-averaged wavelengths and amplitudes L_y and A_y.

Finally, alongshore migration rates were obtained during crescentic bar presence by comparing barlines using cross-correlation. For each barline that is part of a crescentic bar event, the shifted barlines (see example in Figure SI-1 of the Supporting Information, SI) dating between 2 and 4 days after the original barline were identified (under

the condition that the original and shifted barlines belonged to the same crescentic bar event). Subsequently, all shifted barlines were separately cross-correlated with the original barline. The alongshore migrated distance of the crescentic pattern is given by the magnitude of the lag at the positive peak that is located nearest to the origin of the cross-correlogram. The sign of the lag indicates the migration direction (positive for eastward migration). A minimum normalized correlation of 0.7 was imposed. To obtain the migration velocity C_y, the migrated distance is divided by the time difference between the two correlated barlines.

3.3 | Waves

Hourly wave conditions (both integrated wave parameters and 2D spectra) were taken from the SWAN output point located at 10 m

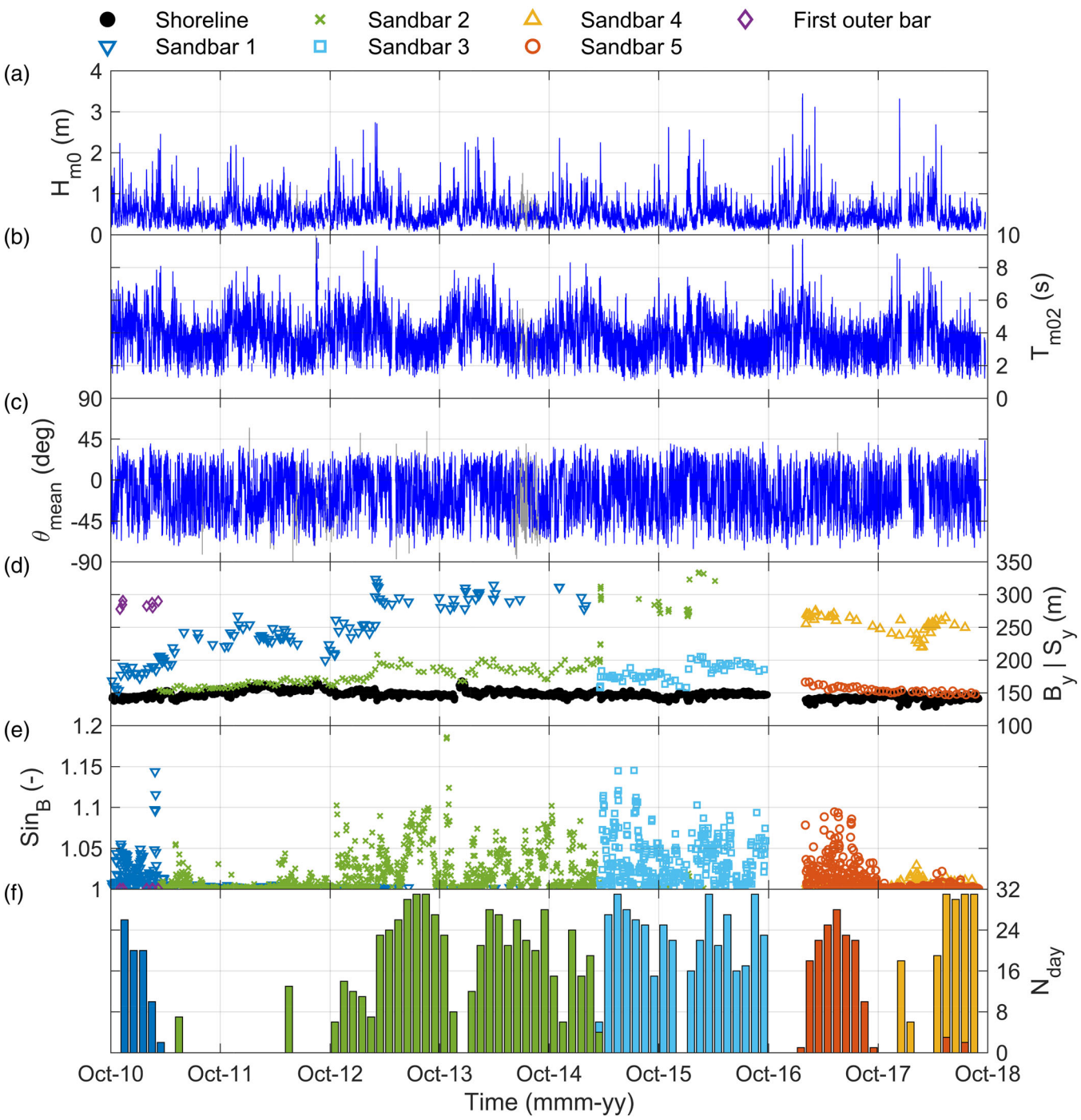

FIGURE 4 (a) Significant wave height H_{m0}, (b) mean period T_{m02}, (c) mean wave direction θ_{mean} from shore-normal (positive for westerly waves), (d) alongshore-averaged bar crest and shoreline positions B_y and S_y, (e) sinuosity of the barlines Sin_B and (f) number of days per month with crescentic bars N_{day} versus time at Castelldefels beach. Panels (a), (b) and (c) display all hourly wave conditions at 10 m depth in front of the study site (no threshold in H_{m0}) and the colours denote the SWAN boundary conditions: 2D spectra (blue) or integrated wave parameters (grey). To increase readability, only a selection of data points of sandbars 1–5 are shown in panel (d). In case crescentic bars occurred in two different sandbars during the same month (e.g., May and July 2018), the bar with the least number of days with crescentic bars is shown at the front in panel (f)

depth in front of the study site (Figure 1). For each barline, the wave conditions in the 24 h prior to midday on the day of the barline were kept. Barlines for which wave conditions were unavailable more than 75% of the time or H_{m0} < 0.2 m were not included in the analysis. Data from the simulation forced with integrated wave parameters was used in presenting the dataset for illustrative purposes (grey data in Figures 4a–c and 5f) but not included in the analysis of the barlines because the wave angle is unreliable

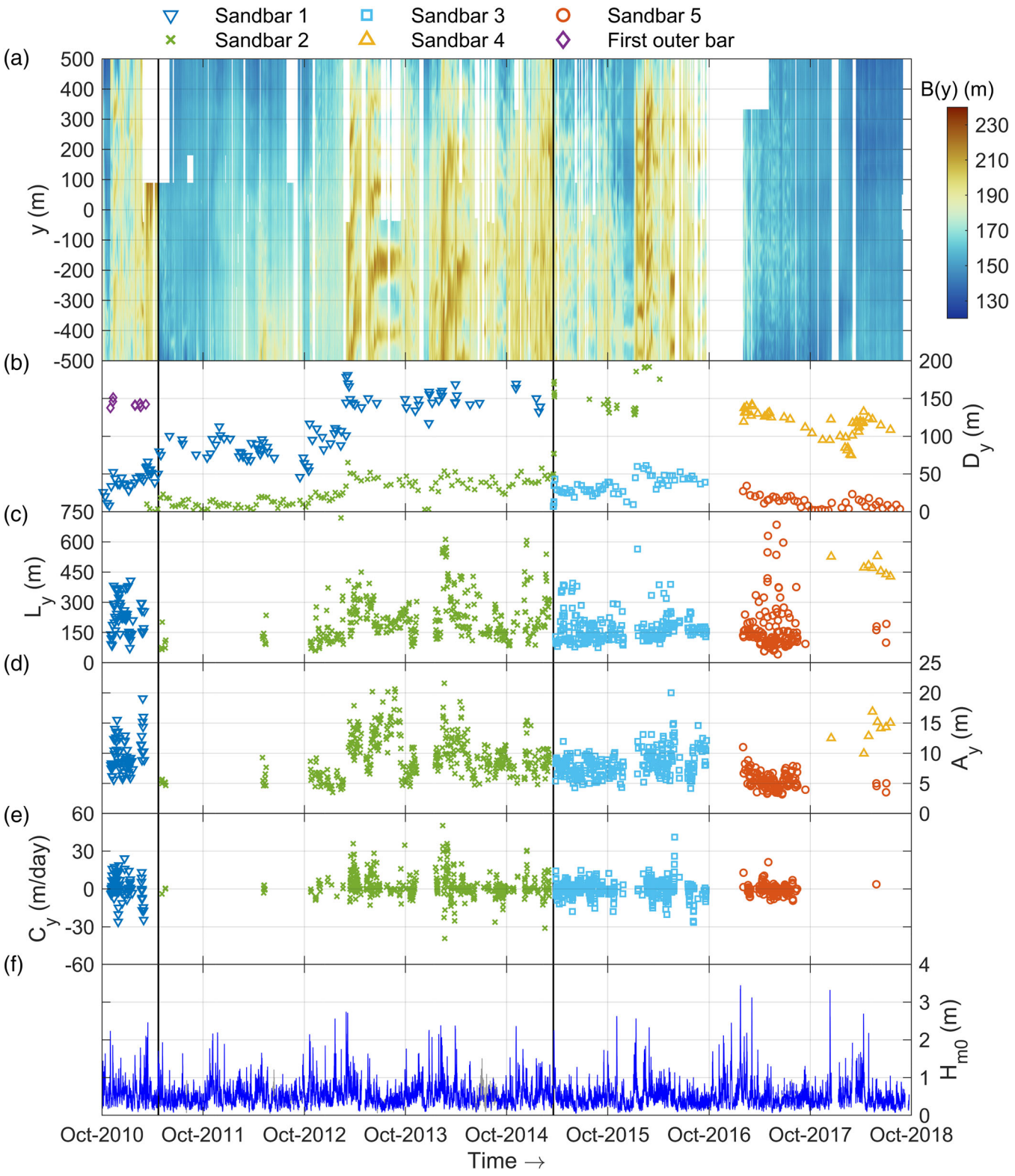

FIGURE 5 (a) Cross-shore bar crest positions (with respect to the camera tower) B at alongshore position y of the bar closest to shore (timestack), (b) alongshore-averaged sandbar–shoreline distance D_y, (c) alongshore-averaged wavelength L_y, (d) alongshore-averaged amplitude A_y, (e) average migration speed C_y (positive for eastward migration), and (f) hourly significant wave height H_{m0} (10 m depth) versus time at Castelldefels beach. The black vertical lines indicate the separation between different sandbars in panel (a). To increase readability, only a selection of data points of sandbars 1–5 are shown in panel (b). Panel (f) displays all hourly wave heights (without threshold) and the colours denote the SWAN boundary conditions: 2D spectra (blue) or integrated wave parameters (grey)

(De Swart et al., 2020). The analysis is thus fully based on SWAN simulations forced by 2D spectra. Wave angles were taken with respect to the shore-normal using a constant coastline orientation of 89° with respect to north. The boundary in wave angle to discriminate between easterly and westerly waves was set at −5° with respect to shore-normal (negative angle indicates east). This adjustment was made because the propagated easterly waves had a negative bias in wave direction of −7.5°, while the westerly waves had a positive bias of 2.3° (De Swart et al., 2020). The alongshore component of the radiation stresses (S_{xy}) was computed using the wave conditions as: $S_{xy} = \frac{c_g}{c}\cos\theta \sin\theta \, \frac{1}{8}\rho g H_{rms}^2$ (Holthuijsen, 2007), where c_g is the group velocity, c is the phase velocity, θ is the wave angle with respect to the shore-normal, ρ is the water density, g is the gravity acceleration and H_{rms} is the root-mean-square wave height $\left(H_{rms} = \frac{H_{m0}}{\sqrt{2}}\right)$. Storms were detected in the measurements of the Barcelona buoy following the criteria set by Ojeda and Guillén (2008), where a storm was defined as a period of at least 12 h during which H_{m0} exceeded 1.5 m and the peak H_{m0} exceeded 2.5 m. When the time between two storms was less than 6 h, it was considered a single double-peaked storm.

4 | RESULTS

4.1 | Alongshore-averaged barline and shoreline positions

A total of six sandbars (always two at the same moment in time) were tracked during the study period (Figure 4d,e). It was decided to treat the sandbars after the gap without images (October 2016 to January 2017) separately and not link them to the sandbars before the data gap, because several storms occurred during this period (Figure 4a), meaning that the real number of studied sandbars might be less than six. The cross-shore position of the shoreline was very stable during the entire period (Figure 4d) and no long-term or seasonal trend in erosion/accretion was observed. In contrast, the cross-shore positions of the sandbars showed a lot of variability with rapid offshore migration during storms and slower onshore movement during post-storm conditions (Figure 4d). The formation of a new sandbar at the shoreline was observed twice (in February 2011 and March 2015) and two episodes of bar disappearance also occurred (in March–April 2011 and March 2015).

Major changes in the average cross-shore sandbar positions were always related to high-energetic wave conditions. Very fast offshore migration (70 m in 1 day) was observed in March 2013 and March 2015 (details in Figure SI-2). Other cases of fast offshore migration (up to 40 m/day) were observed in November 2010, January 2011, April 2011, November 2011, March 2012, October 2012, December 2013 and January 2016 (Figure 4d). In April 2011 and March 2015, the original inner bar migrated offshore and became the new outer bar (sandbar 1 and sandbar 2, respectively). This in turn allowed for a new or recently formed sandbar (sandbar 2 and sandbar 3, respectively) to occupy the location left by the migrated original inner bar. Moreover, the original outer bar (first outer bar and sandbar 1, respectively) moved further offshore (outside the planview domain), so that waves were no longer breaking on them and they probably slowly diffused (as reported at other coasts by Ruessink & Kroon, 1994 and Shand et al., 1999). Note also that the remnants of a previous outer bar are visible at deeper water in two of the profiles in Figure 2 (around cross-shore coordinate 480 m).

TABLE 1 Yearly statistics of crescentic bar occurrence and mean bar characteristics (mean absolute values for C_y) for each tracked sandbar during the entire study period. Statistics are also given for all inner and outer bar data. A crescentic bar event that occurs within 2 years is ranked among the year in which the event started. Years without crescentic bars in the respective sandbar are not displayed

Sandbar	Year	Number of events	Mean duration (days)	Total duration (days)	D_y (m)	L_y (m)	A_y (m)	C_y (m/day)
Sandbar 1	2010[a]	6	11	66	32	233	9	5.6
	2011	1	12	12	64	212	13	9.8
Sandbar 2	2011	2	3.5	7	9	105	5	1.4
	2012	10	4.5	45	12	135	6	3.7
	2013	16	15	241	36	223	11	5.6
	2014	15	17	250	38	241	10	6.0
	2015	5	7.6	38	64	253	8	5.8
Sandbar 3	2015	12	17	205	28	159	8	3.6
	2016[b]	9	23	204	44	173	9	4.9
Sandbar 4	2017[c]	1	24	24	122	527	12	–
	2018[d,e]	1	142	142	110	468	14	–
Sandbar 5	2017[c]	18	8.3	150	14	167	5	1.9
	2018[d]	2	2.5	5	8	159	5	3.7
Inner bar (complete)	2010–2018	96	13	1223	33	196	9	4.7
Outer bar (complete)	2010–2018	2	83	166	119	475	14	–

[a]Only data for October-December 2010.
[b]No data for October–December 2016.
[c]No data for January 2017.
[d]No data for September–December 2018.
[e]Event extends beyond study period.

4.2 | Crescentic bar occurrence

A total of 98 crescentic bar events were observed in the study period (Table 1), of which 96 occurred in the inner bar and two in the outer bar. In total, crescentic bars were present during 48% of the time (1389 days). No seasonal signal is present in the occurrence of crescentic bars, but there is a clear uneven distribution in presence over the different years (Figures 4f and 5a). Crescentic bars were often present during 2013–2017, whilst in 2011–2012 there were long periods without any crescentic bar (Table 1). There are also significant differences in event duration between the different years (varying from days to months). It is important to bear in mind that crescentic bars at Castelldefels can retain their configuration for a long time during extended periods with low-energetic wave conditions. This leads

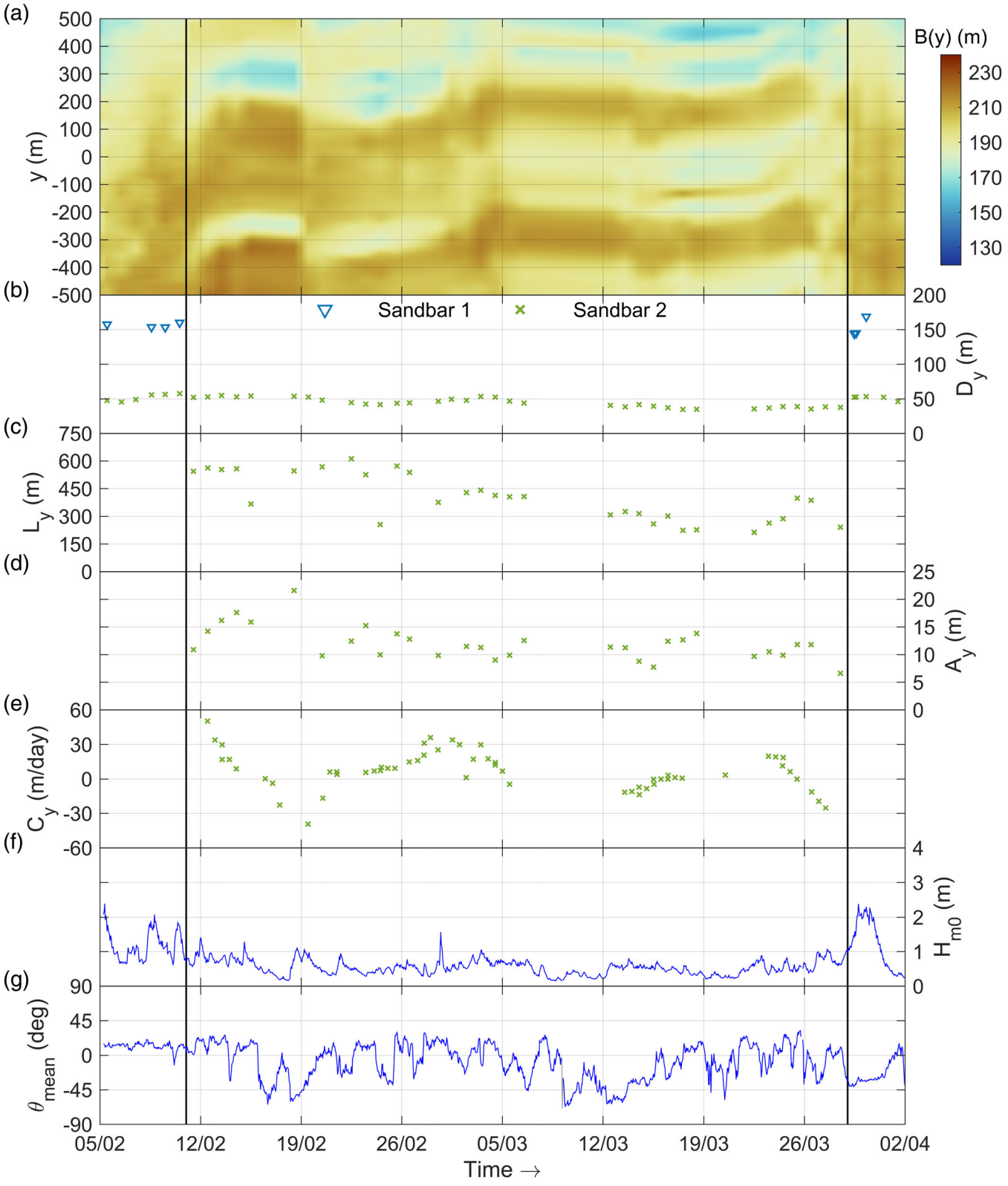

FIGURE 6 Identical to Figure 5, but now for one clear crescentic bar event in February–April 2014. Additionally, the mean wave direction θ_{mean} from shore-normal (positive for westerly waves) at 10 m depth is added in panel (g). Panels (f) and (g) display all hourly wave conditions (no threshold in H_{m0}) and the black vertical lines indicate the start and end of the crescentic bar event

to freezing of the morphological configuration (bar arrestment; Ojeda et al., 2011) until the wave energy increases. A nice example occurs in summer 2013 (Figure 5a).

The uneven distribution of crescentic bars over the different years turns out to be related to changes in the alongshore-averaged sandbar–shoreline distance (Figure 4d,f). Crescentic bars developed frequently when the sandbar was located at least a certain distance from the shoreline (10–15 m). When the sandbar was located too close to shore, it did not become crescentic. Also, nearly all crescentic bar events occurred in the inner bar, meaning that the sandbar should not be located too far from shore either. The reason is that if the bar is at deeper water morphological changes can only occur during high-energetic wave conditions.

4.3 | Crescentic bar formation/straightening

A large number of crescentic bar formation/straightening moments occurred during the study period. Examples of planviews during formation and straightening for a characteristic crescentic bar event have already been shown in Figure 3. The corresponding time series of the same crescentic bar event are shown in Figure 6.

At the study site, crescentic bars developed in periods with relatively calm wave conditions and not very oblique angles of incidence that followed after a short period with medium–high energetic wave conditions (e.g., Figure 6 on 10 February 2014). As mentioned in the previous section, the sandbar should also be located at a sufficient distance from shore. As long as the wave conditions remained calm, the crescentic bars continued to grow and develop more pronounced undulations. When the wave direction became more oblique, this could lead to alongshore migration (e.g., Figure 6 between 19 February 2014 and 5 March 2014). The crescentic pattern was typically destroyed during storms with medium–high energetic wave conditions and strong oblique angles of incidence (e.g., Figure 6 on 28–29 March 2014), although sometimes bar straightening was caused by the sandbar welding to the shoreline. During really low-energetic wave conditions (hardly any breaking), no morphological changes were observed and bar arrestment occurred (e.g., between 6 March 2014 and 12 March 2014 in Figure 6). Crescentic bars were often accompanied by undulations at the shoreline (megacusps), which mostly developed 1–2 days after the formation of a crescentic bar but sometimes developed halfway through a long-lasting crescentic bar event (Figures 3d and SI-3). They typically continued to grow as long as low-energetic wave conditions persisted and mostly disappeared with crescentic bars during storms.

Histograms of the wave height and wave direction are shown in Figure 7 for six categories: the entire study period (a), days with crescentic bar presence (b), formation moments (c), straightening moments (f), days without crescentic bars (d) and days without crescentic bars but sufficient bar–shoreline distance (e). The bar was assumed to be located at a sufficient distance from shore for the formation of crescentic bars if D_y > 10 m, which was chosen after analysing D_y for all moments with crescentic bars. Standard deviations are indicated in Figure 7 with crosses located at the median. Due to the clear bimodal distributions, the statistical parameters of the wave angle in Figure 7d–f are computed separately for easterly and westerly waves using a boundary of $-5°$ (as justified in the Methods section). Additional statistics of the wave conditions for all categories are given in Table 2.

Figure 7a and Table 2 again emphasize that low–medium energetic wave conditions with a large variety in wave angle dominated during the study period. Similar wave conditions dominated when no crescentic bars were present (Figure 7d). In contrast, high-energetic waves were completely absent during the presence of crescentic bars

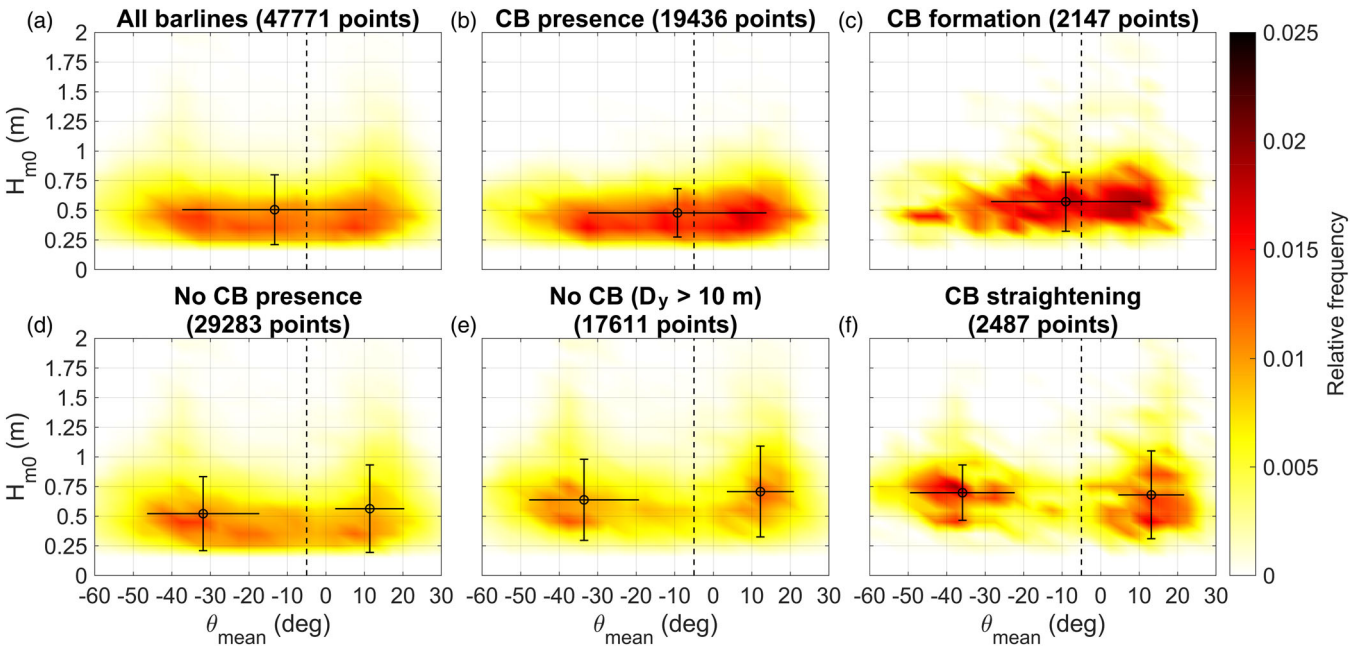

FIGURE 7 2D histograms of hourly significant wave height H_{m0} versus hourly mean wave direction θ_{mean} from shore normal (positive for westerly waves) at 10 m depth for different categories (CB denotes crescentic bar). Only data from the simulation forced with 2D spectra are shown and waves with H_{m0} < 0.2 m are excluded. The error bars intersect at the median and indicate the standard deviation of both wave parameters. The dashed vertical line is the separation between easterly and westerly waves for computing the error bars/medians of θ_{mean} in panels (d), (e) and (f)

TABLE 2 Statistical values (mean, standard deviation) of integrated wave parameters at 10 m depth in front of Castelldefels beach for the categories in Figures 7 and 8

	H_{m0} (m)		T_{m02} (s)		θ_{mean} (deg)		θ_{mean} (east) (deg)		θ_{mean} (west) (deg)	
Category	Mean	SD	Mean	SD	Mean	SD	Mean	SD	Mean	SD
All barlines (a)	0.57	0.29	4.0	1.1	−14	24	–		–	–
CB presence (b)	0.51	0.20	3.8	0.96	−12	23	–	–	–	–
CB formation (c)	0.61	0.25	4.4	0.94	−11	19	–	–	–	–
No CB presence (d)	0.62	0.34	4.2	1.2	–	–	−31	15	11	9
No CB (D_y > 10 m) (e)	0.74	0.36	4.5	1.2	–	–	−32	14	12	9
CB straightening (f)	0.73	0.31	4.4	1.1	–	–	−34	14	13	9

Note: The final letters in the first column refer to the panels of Figures 7 and 8. Depending on the distribution in Figure 7, the statistics of θ_{mean} (with respect to shore-normal) have either been evaluated separately for easterly and westerly waves (separation at −5° from shore-normal) or for all waves combined. Statistics are computed using the simulation forced with 2D spectra and excluding waves with H_{m0} < 0.2 m.

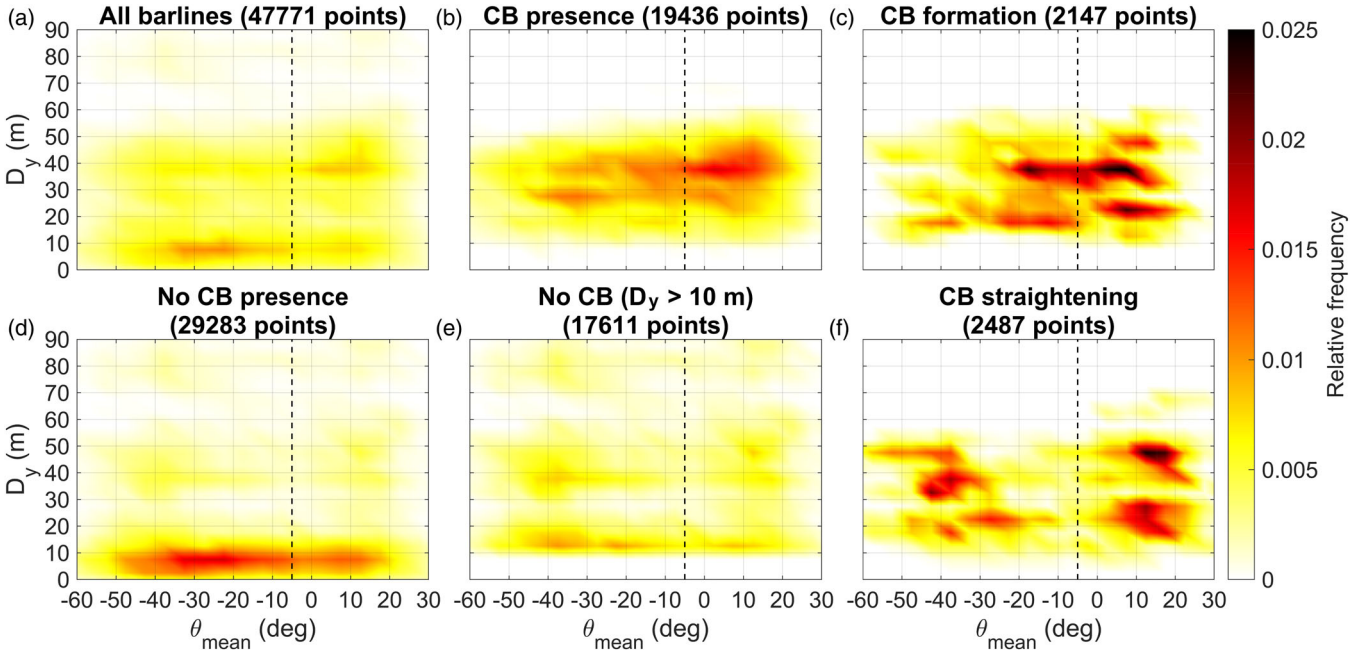

FIGURE 8 2D histograms of the average bar–shoreline distance D_y versus hourly mean wave direction θ_{mean} from shore normal (positive for westerly waves) for different categories (similar to those in Figure 7). Only data from the simulation forced with 2D spectra is shown and waves with H_{m0} < 0.2 m are excluded

and the waves were slightly less oblique (Figure 7b). During crescentic bar formation (Figure 7c and Table 2), a litte more energetic waves prevailed and the wave angles were less oblique compared to the rest of the categories. Consistently, south-southwesterly and bimodal wave climates were dominant (Figure SI-4) and east-southeasterly wave climates (generally characterized by more oblique wave directions) occurred less frequently. During crescentic bar straightening (Figure 7f), oblique waves were clearly dominant and shore-normal waves were rare (south-southwesterly and east-southeasterly wave climates prevailed; Figure SI-4). Furthermore, high-energetic wave conditions occurred quite frequently (particularly for southwesterly waves). Nearly identical wave conditions were seen when the bar–shoreline distance was sufficient but no crescentic bar occurred (Figure 7e).

The relation between crescentic bar occurrence and the bar–shoreline distance is further demonstrated in Figure 8. It is clear that crescentic bars were mostly present for bar–shoreline distances between 20 and 50 m (Figure 8b), whereas they were absent when the bar was located close to shore (D_y < 10 m; Figure 8d). Also, when the bar was sufficiently offshore (D_y > 10 m) but no crescentic bar was present, the bar was generally still fairly close to the shoreline (between 10 and 20 m; Figure 8e). Finally, crescentic bar formation and straightening (Figures 8c,f) generally occurred when the bar was located between 15 and 50 m from the shore (comparable to crescentic bar presence). Compared to Figure 8b, Figures 8c,f show a certain scattering, which is due to the fewer data points in those last two figures.

4.4 | Crescentic bar characteristics

Crescentic bar characteristics varied a lot during the same event (Figures 5c–e and 6c–e). Substantial differences in average crescentic bar wavelengths were observed for the same sandbar between

different years and also between the various sandbars (Table 1). The early stages of longer-lasting (more than 1 week) crescentic bar events were often characterized by relatively large wavelengths (L_y above 400 m). As the crescentic bars developed further, the wavelengths often decreased (L_y below 300 m) due to splitting of individual crescents (compare the wavelength on 13 February 2014 with the wavelengths on 5 March and 18 March 2014; Figure 6c). At the end of the event, the wavelengths often increased again as the smaller intermediate undulations disappeared prior to the larger undulations (compare the wavelengths on 18 March and 26 March 2014; Figure 6c). In contrast, the wavelengths of short-term (less than 1 week) events were mostly quite small (L_y below 300 m) and generally quite constant throughout the entire event. The amplitudes showed a more limited variability. The early stages of a crescentic bar event were often characterized by small amplitudes (A_y of the order of 5 m), which typically increased during longer-lasting events (compare the amplitudes on 11 February and 18 February 2014; Figure 6d) and could reach values of 20 m. Alongshore migration speeds were typically quite small (C_y between −10 and +10 m/day), and larger migration speeds were mostly observed for more pronounced (longer-lasting) crescentic bar events with larger wavelengths and amplitudes (Figures 5e and 6e).

The large variability in wavelength is partly related to the aforementioned splitting and merging of individual crescents, but the wavelength also tends to increase with the bar–shoreline distance (Figure 9). Despite the scatter and the relatively low correlation coefficient, the relation is highly significant at the 99% confidence level. In agreement with the observed trend in the inner bar, constant large wavelengths were observed during the only two crescentic bar events in the outer bar (Table 1 and Figure 5c). Finally, a clear relation is present between the migration speed magnitudes and the alongshore radiation stress S_{xy} (Figure 10). The observed trend does not depend very much on the time period over which the migration speeds were computed (as explained in the Methods section) since similar linear fits and correlation coefficients were found for the different time periods and all relations are highly significant at the 99% confidence level.

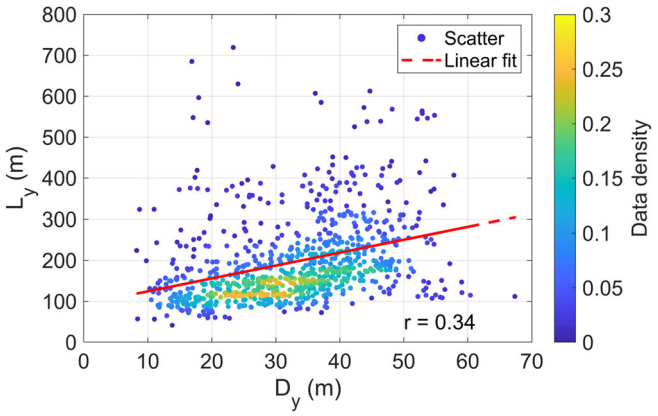

FIGURE 9 Average wavelength L_y versus average bar–shoreline distance D_y for all inner bar data including linear fit and Pearson correlation coefficient. Colours denote the data density

5 | DISCUSSION

5.1 | Accuracy of crescentic bar detection

Crescentic bar events and specifically the formation/straightening moments were detected visually in this study (analogous to Holman

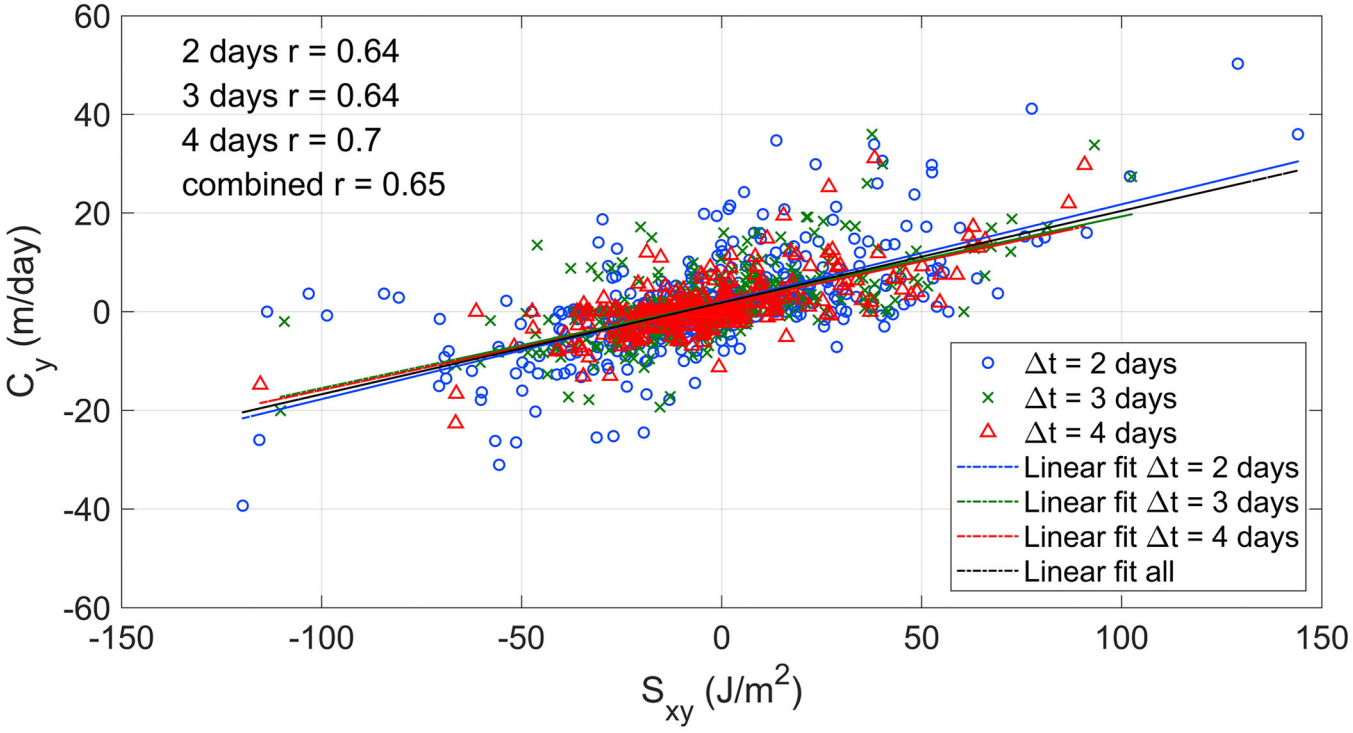

FIGURE 10 Average crescentic bar migration speed C_y (positive for eastward migration) versus alongshore radiation stress S_{xy} (positive for waves coming from the west). Linear fits and the corresponding Pearson correlation coefficients are also included. The different colours indicate the time period over which the migration speed was computed. For each migration speed, S_{xy} was averaged over the corresponding time period. When computing S_{xy}, the bias in wave direction was compensated by adding 5° to the wave angles (see the Methods section)

et al., 2006) by two experienced researchers to prevent bias and increase accuracy. However, previous studies on crescentic bars often employed an automatic algorithm using either the standard deviation of the detrended barline (σ_B; e.g., Contardo & Symonds, 2015; Price & Ruessink, 2011) or the sinuosity of the barline (Sin_B; Ojeda et al., 2011). In order to test the reliability of these two parameters, the values of σ_B and Sin_B at Castelldefels were plotted for the moments with and without visually detected crescentic bars (Figure 11). Clearly, Sin_B works better as a proxy for crescentic bar presence (e.g., $Sin_B \gtrsim 1.01$) than σ_B, but there is still a substantial range in Sin_B for which this parameter is inconclusive. In particular, crescentic bars could be present for $Sin_B = 1.005$–1.01 and not exist for $Sin_B = 1.01$–1.02. Since Sin_B does not discriminate well enough, it was decided to use the visual analysis to obtain maximum accuracy.

Visual detection of straightening moments was generally quite clear because they mostly occurred within 1 day. Detecting formation moments was more challenging, since they were generally more subtle and could take longer than 1 day. An additional complication is the inertia (hysteresis) of the system, meaning that the previous morphological configuration affects the time needed for formation and, especially, straightening. Other reasons that explain the noise in Figures 7 and 8 are (i) the visual analysis was done with one daily image (at 12:00) instead of hourly images, and (ii) crescentic patterns were sometimes only present in one half of the planview domain with the bar–shoreline distances differing substantially in the planview, meaning that the alongshore-averaged bar–shoreline distance was not fully representative. Finally, the wave conditions that occurred in the 24 h before midday were considered for each BLIM image. However, since formation (straightening) could take more (less) than 24 h, an excess (lack) of wave conditions could be considered regarding formation (straightening). Sensitivity was checked and Figures 7 and 8 hardly change when decreasing the number of hours to 18 or 12.

5.2 | Comparison with previous observations

A strong result of this study is that the initial bathymetry plays an important role in the formation of crescentic bars. Crescentic bars were only observed when the bar–shoreline distance exceeded 10–15 m (Figures 8b and 12) and they were hardly observed when the bar–shoreline distance exceeded 60 m (Figures 8b and 12). Previous studies (Contardo & Symonds, 2015; Holman et al., 2006) also reported that initial bathymetric conditions strongly influenced crescentic bar dynamics. Other characteristics of the cross-shore inner bar profile at the study site are unfortunately unknown, because the topobathymetry was at most surveyed every 6 months and the inner bar profile was often not measured. The last 3 surveys indicate that an inner terrace instead of an inner bar can occur at the study site (Figure 2), meaning that the inner barlines tracked with BLIM might often reflect terrace edges instead of real bars.

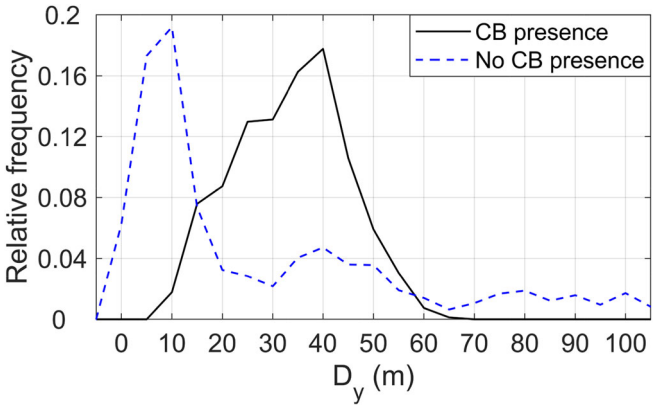

FIGURE 12 Distribution of bar–shoreline distance D_y on days with and without crescentic bar presence

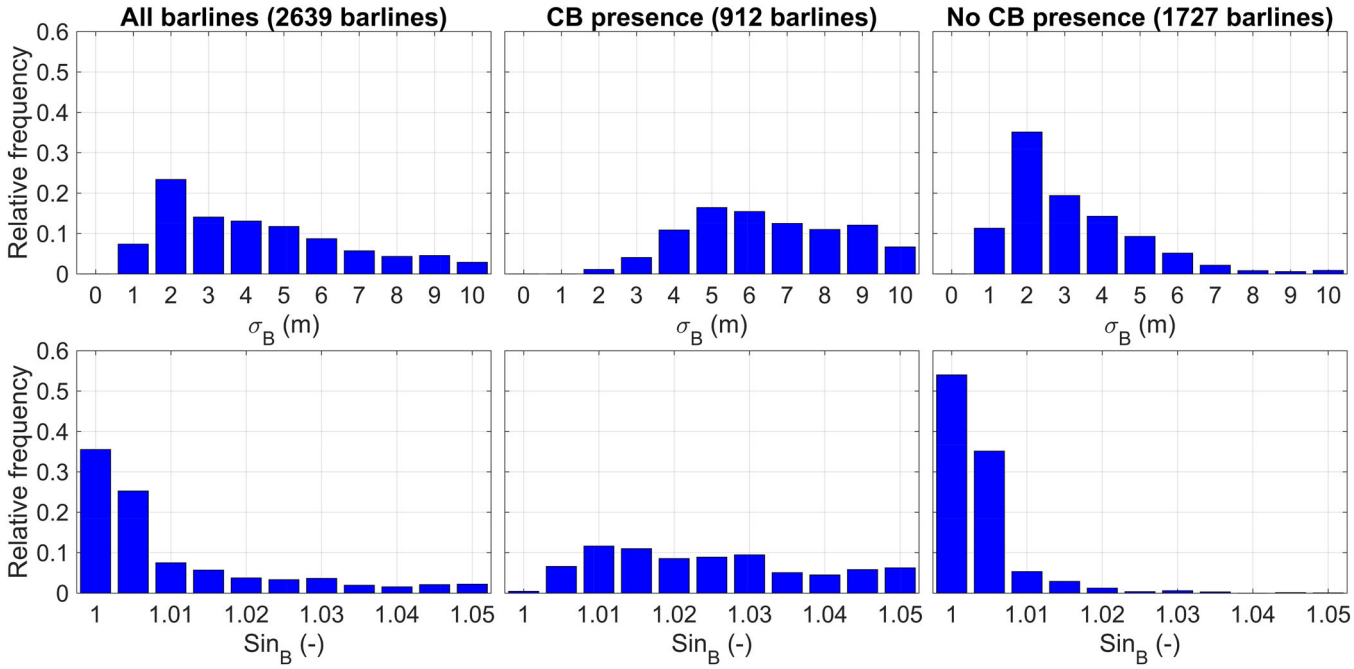

FIGURE 11 Histograms of the standard deviation of the barline σ_B (top) and the sinuosity of the barline Sin_B (bottom) for all barlines (left), all barlines with visually detected crescentic bars (middle) and without visually detected crescentic bars (right)

At the study site, crescentic bars were only observed in the outer bar during 2017–2018, when a few strong storms caused a change in bar configuration. The bar was arrested between the storms, which explains the long crescentic bar events in 2018 (Figure 4f and Table 1). The inner bar was only arrested during very low-energetic wave conditions (H_{m0} < 0.2 m) that were excluded from our data and mostly occurred during summer (e.g., during summer 2013; Figure 5). Similar observations were made at other Mediterranean beaches (e.g., Ojeda et al., 2011).

The large number of observed crescentic bar events allowed for a detailed analysis of the wave conditions during crescentic bar presence and formation/straightening moments. From now on, the mentioned wave angles are taken with respect to the boundary of -5° at 10 m depth (see Methods). Analysing the wave conditions reveals that during crescentic bar straightening (Figures 7f and 13a and Table 2) oblique waves were dominant (on average $\theta_{mean} \gtrsim 15^\circ$ at 10 m depth) and shore-normal waves were mostly absent. Furthermore, the waves were more energetic than during crescentic bar formation/presence (mean H_{m0} of 0.73) and there was more variation in wave height (Figure 13b). This indicates that bar straightening occurred during medium- and high-energetic oblique wave conditions. Waves were generally low energetic during crescentic bar formation and crescentic bar presence (mean H_{m0} < 0.6 m; Figures 7b,c and 13b and Table 2). Clearly, the wave angles during formation were less oblique (mostly $\theta_{mean} \lesssim 20^\circ$) and formation was often observed for shore-normal waves (Figure 13a). The wave climates during crescentic bar formation were mostly south-southwesterly and bimodal (since these typically showed smaller angles of incidence), whereas south-southwesterly and east-southeasterly wave climates dominated during crescentic bar straightening (Figure SI-4). Consistent with the lack of bimodal wave climates during crescentic bar straightening, the directional spreading in those moments was relatively small (Figure SI-5).

Crescentic bar formation has been observed to occur in the field both during calm and more energetic wave conditions with relatively small angles of incidence (e.g., Gijsman et al., 2021; Price & Ruessink, 2011; Rutten et al., 2018). At Castelldefels, mostly low-energetic wave conditions were observed during formation (Figure 7c) and the angles were 10–20° less oblique compared to the straightening moments (Figure 7f). Still, the angles show a wide range (from -30° to $+20^\circ$ at 10 m depth). Previous studies (Contardo & Symonds, 2015; Gijsman et al., 2021) reported crescentic bar development for angles up to 9° (at 10 m depth), while Price and Ruessink (2011) observed downstate (accretionary) transitions in the classification scheme of Wright and Short (1984) for angles up to 23° (at 10 m depth). Crescentic bar straightening was previously mainly related to storm conditions (e.g., Ranasinghe et al., 2004; Van Enckevort et al., 2004), while later studies (Holman et al., 2006; Price & Ruessink, 2011) related sandbar straightening more to oblique waves. Consistent with several recent studies (Contardo & Symonds, 2015; Gijsman et al., 2021; Rutten et al., 2018), sandbar straightening at Castelldefels predominantly occurred during oblique waves while shore-normal waves were almost absent (Figure 7f).

At the study site, mean wavelengths varied between 100 and 700 m (Figure 5c) and mean amplitudes between 5 and 20 m (Figure 5d). Yearly averages (Table 1) were smaller compared to most previous studies (Table 3), which could be related to the small tidal action and low-energetic wave conditions at the study site. However, previous Mediterranean studies (e.g., Bouvier et al., 2017; Gervais et al., 2011) reported larger wavelengths and amplitudes, which might be related to larger bar–shoreline distances. At Castelldefels, the wavelength increased for larger bar–shoreline distances (Figure 9) and similar trends are seen in Table 3 for other sites. Alongshore migration rates at Castelldefels could reach up to 50 m/day (Figure 5e), but yearly averages were mostly around 5 m/day (Table 1). Migration rates were strongly related to the alongshore component of the radiation stresses S_{xy} (Figure 10). Comparable relationships were found previously (Holman et al., 2006; Ruessink et al., 2000), using the longshore component of wave energy flux or a mean alongshore current proxy, respectively. Similar to Holman et al. (2006), the relationship became more significant for longer time spans.

Several moments of fast offshore migration with rates of 20–70 m/day were observed at the study site in response to high-energetic waves (Figure 4d), two of which resulted in the formation of a new inner bar. This behaviour is very similar to the episodic net offshore migration (NOM), first described by Ruessink et al. (2009) at the Gold Coast (cross-shore migration up to 30 m/day), and strongly resembles the observed offshore sandbar migration patterns at the low-energetic Italian beach of Terracina (Melito et al., 2020; Parlagreco et al., 2019). NOM patterns were also reported along the low-energetic French Mediterranean coast (Sète beach), both

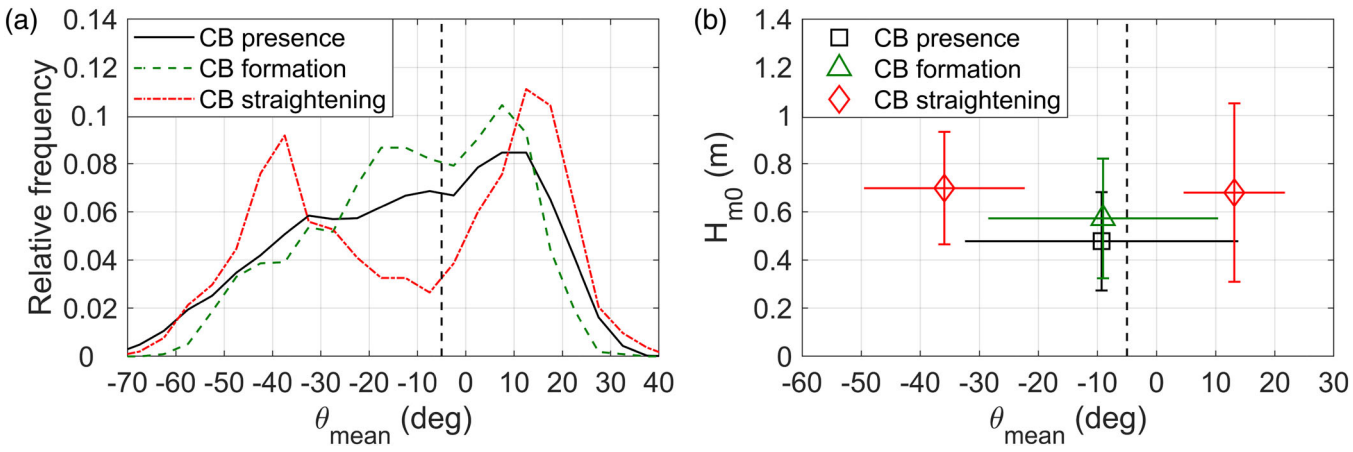

FIGURE 13 Distributions of θ_{mean} at 10 m depth during crescentic bar presence/formation/straightening (a) and the error bars of the same categories (taken from Figure 7b,c,f) collected together to facilitate comparison (b)

TABLE 3 Overview of several recent crescentic bar and rip-channel observations displaying both site and bar characteristics. All columns show mean values except tides (spring tidal range) and C_y (mean absolute value and absolute range). A comprehensive overview of earlier crescentic bar observations is given in Table 1 of Van Enckevort *et al*. (2004)

Site	D_{50} (μm)	Slope	Tide (m)	H_{m0} (m)	L_y (m)	A_y (m)	C_y (m/day)	Study period	Reference
Leucate-Plage[1]	600	0.015	0.3	0.8	300	–	– (0.1–0.3)	≈2 years[b]	Certain (2002)
Leucate-Plage[2]	600	0.015	0.3	0.8	600	–	≈ 0.1 (–)	≈2 years[b]	Certain (2002)
Duck	180	0.013	1.1	0.89	365	24	– (0–60)	2 months[a]	Van Enckevort et al. (2004)
Miyazaki	250	0.013	1.6	1.29	363	34	– (0–50)	2 months[a]	Van Enckevort et al. (2004)
Gold Coast[1]	250	0.02	1.7	1.10	373	15	– (0–45)	3 months[a]	Van Enckevort et al. (2004)
Gold Coast[2]	250	0.02	1.7	1.10	483	24	– (0–35)	3 months[a]	Van Enckevort et al. (2004)
Noordwijk[1]	170	0.007	1.8	1.05	871	36	– (0–60)	10 months[a]	Van Enckevort et al. (2004)
Noordwijk[2]	170	0.007	1.8	1.05	1369	43	– (0–25)	10 months[a]	Van Enckevort et al. (2004)
Palm Beach	300	0.02	1.0	1.5	178	–	2.4 (0–21)	4 years[a]	Holman et al. (2006)
Truc Vert[1]	300	0.02	5.0	1.3	400	–	2.5 (0.5–4.3)	3/13 years[b,c]	Castelle et al. (2007)
Truc Vert[2]	300	0.02	5.0	1.3	700	–	1.0 (–)	3/13 years[b,c]	Castelle et al. (2007)
Monterey Bay	250	0.01	1.5	≈ 2.0	≈ 300	–	≈ 7.0 (0–30)	1–3 years[a]	Orzech et al. (2010)
Gulf of Mexico[1]	–	–	< 0.5	0.85	≈ 500	–	– (–)	1–2 years[b]	Arifin and Kennedy (2011)
Gulf of Mexico[2]	–	–	< 0.5	0.85	> 1000	–	– (–)	1–2 years[b]	Arifin and Kennedy (2011)
Lido di Dante	215	0.03	0.9	≈ 0.7	256	-	– (–)	4.5 years[a]	Armaroli and Ciavola (2011)
Sète	200	0.09	0.3	0.7	≈ 300	≈ 40	– (–)	4 months[a,b]	Gervais et al. (2011)
Perranporth	350	0.012	6.3	1.5	363	–	– (–)	6 years[a,b]	Scott et al. (2014)
Sète	200	0.09	0.2	0.5	≈ 400	–	– (0–150)	5 years[a]	Bouvier et al. (2017)
Anmok	400	0.02	0.3	1.1	383	45	– (–)	27 years[c]	Athanasiou et al. (2018)
Zandmotor[3]	280	0.013	1.7	0.97	≈ 200	–	– (–)	2.4 years[a]	Rutten et al. (2018)
Zandmotor[4]	280	0.013	1.7	0.97	≈ 450	–	– (–)	2.4 years[a]	Rutten et al. (2018)
Sylt[3]	360	0.033	2.0	≈ 0.9	670	–	– (–)	40 years[b]	Gijsman et al. (2021)
Sylt[4]	360	0.022	2.0	≈ 0.9	2240	–	0.2 (–)	40 years[b]	Gijsman et al. (2021)
Castelldefels[1]	270	0.014	0.2	0.57	196	9	4.7 (0–50)	≈ 8 years[a]	This study
Castelldefels[2]	270	0.014	0.2	0.57	475	14	– (–)	≈ 8 years[a]	This study

Note: Sandbar detail: [1]inner bar; [2]outer bar; [3]northern part; [4]western/southern part. Main dataset: [a]video data; [b]bathymetric data; [c]satellite data.

interannually (e.g., Aleman et al., 2017) and episodically (up to 50 m/day Bouvier et al., 2017). At Castelldefels, fast offshore migration only occurred during storms, but there were also many storms without significant cross-shore migration. This suggests that the underlying bathymetry also plays an important role in the occurrence of NOM patterns at Castelldefels. Previous studies suggested that NOM patterns also depend on bar steepness and bed slopes (Melito et al., 2020; Parlagreco et al., 2019) and on bar volumes (Ruessink et al., 2009). However, the lack of bathymetric data at Castelldefels makes it impossible to investigate this in detail.

5.3 | Comparison with previous model studies

Some modelling studies investigated the importance of the initial bathymetry in crescentic bar formation. On single-bar profiles, models predict that wavelengths increase with bar–shoreline distance (Calvete et al., 2007; Damgaard et al., 2002). However, other bathymetric characteristics (such as bar trough/crest depths and the bed slope) also have a strong effect on the wavelength (Calvete et al., 2007), but they are generally unknown at Castelldefels. This is the most probable explanation for the large variation in inner bar wavelength as a function of bar–shoreline distance in Figure 9. The observed important role of bar–shoreline distance on crescentic bar presence in Castelldefels (minimum distance of 10–15 m) remains unexplained by existing modelling studies. In particular, Calvete et al. (2007) found that growth times were not significantly correlated to bar–shoreline distance (Figure 4 in their article) but the range in their study ($65 < D_y < 90$ m) did not include the small bar–shoreline distances in the present data. Moreover, growth times of crescentic bars in terraced beaches strongly increased compared with barred beaches (Calvete et al., 2007), while crescentic bars are likely present when an inner terrace exists at Castelldefels beach. In contrast to single-bar profiles, modelling studies using double-barred profiles systematically predict larger wavelengths in the outer bar compared to the inner bar (Klein & Schuttelaars, 2006; Smit et al., 2008; Thiébot et al., 2012), similar to the observations at Castelldefels.

The role of wave conditions on crescentic bars has also been the subject of many modelling studies. Table 4 provides an overview of such studies in different settings that used wave conditions roughly resembling those at Castelldefels (significant wave height $H_s \leq 2$ m, peak period $T_p \leq 6$ s, wave angle $\theta > 3^\circ$ at 10 m depth). In the absence of any specific study for Castelldefels beach, the results of the studies in Table 4 will be compared to the Castelldefels observations. However, the comparison can only be done qualitatively, as the bathymetries and wave conditions in the models were most of the time

TABLE 4 Overview of model results for crescentic bar formation for comparison with Castelldefels data. Wave conditions are given at 10 m depth and for double-bar studies only values at the inner bar are given. The *e*-folding growth time T_g and saturation time T_s are provided in the model studies, together with the wavelength L_y and migration rate C_y. C_y^{obs} indicates the observed migration speeds that, according to the 2-day linear fit in Figure 10, correspond to the S_{xy} values of the model studies

Profile	D_y (m)	D_{50}	T_p (s)	H_{m0} (m)	θ (deg)	S_{xy} (J/m^2)	T_g (days)	T_s (days)	L_y(m)	C_y (m/day)	C_y^{obs}	Reference
Single bar (Duck, USA)	80	200	6.0	2.0	4.3	126	0.8	–	300	36	27	Calvete et al. (2005)[c]
				2.0	8.6	247	1.0	–	450	60	51	
				2.0	13	362	1.3	–	550	84	73	
				1.9	17	465	1.7	–	700	108	94	
Inner bar[a] (Dutch coast)	130	250	6.0	1.0	8.6	66	0.4	–	600	80	15	Klein and Schuttelaars (2006)
							–	2	1000	100		
Single bar (Duck, USA)	80	250	7.5	1.3	4.2	59	2.8	–	200	22	14	Garnier et al. (2008)[d]
					5.6	79	4.2	30	220	28	18	
Inner bar[a] (Dutch coast)	145	150	6.0	1.0	10	75	–	5	600	–	–	Smit et al. (2008)
Inner bar[b]	50	200	6.5	2.1	5.3	189	2.9	–	200	43	39	Thiébot et al. (2012)
Single bar (Duck, USA)	80	250	6.0	1.4	5.3	74	–	30	250	20	17	Nnafie et al. (2020)[e]

[a]No formation on the outer bar.
[b]Formation also on the outer bar (not shown).
[c]Similar results for $H_s = 1.3$ m.
[d]Similar results for $T_p = 6$ s.
[e]Results for constant θ case.

different from Castelldefels. The inner bar along the Dutch coast and at Duck (USA) is located farther from shore and the wave heights and periods in all model studies are larger compared to the averages (0.6 m and 4 s) at Castelldefels. As shown in Table 4, reported growth times in modelling studies are either the *e*-folding growth time, T_g (time needed to multiply the bar height by a factor *e*) or the saturation time, T_s (time needed for the bar to reach a relatively constant bar height). The observations in Castelldefels, with crescentic foam patterns appearing after 1–2 days, are only comparable to model results with $T_s < 5$ days or $T_g < 1$ days (several amplification cycles are needed before the crescentic bar affects the foam pattern).

The role of wave conditions in modelling studies is in qualitative agreement with observations at Castelldefels, with formation occurring for less oblique waves and straightening occurring for larger angles (wave height playing a minor role), but some details are not completely captured by models. Crescentic bars generally form in models for $\theta < 5^\circ$ at 10 m depth, a value significantly smaller than the observations at Castelldefels. Larger incidence angles either lead to excessively long evolution times, with growth time $T_g > 2$ days or saturation time $T_s > 10$ days, or wavelengths become much larger ($L_y > 500$ m) than those observed at Castelldefels (references in Table 4; see also Castelle and Coco, 2012; Price *et al*. 2013). More advanced models that include directional spreading in the wave forcing (Reniers et al., 2004; Smit et al., 2008) or use a time-variable wave angle (Castelle & Ruessink, 2011; Nnafie et al., 2020, 2021), cross-shore transport (Rutten et al., 2019) or algorithms to evaluate the cumulative effects of waves and their variations (Tiessen et al., 2010), predict formation for larger angles but still fail to reproduce the wide range of angles at which formation occurs at Castelldefels beach. The same applies to crescentic bar straightening, which is observed for angles much larger than those predicted by models (Garnier et al., 2013).

Once formed, crescentic bars experience both alongshore migration and changes in wavelength due to splitting and merging. In order to test the migration rates reported in existing modelling studies, Figure 10 has been used to compute the observed migration rate corresponding to the S_{xy} values implemented in the models (Table 4). Most models (Calvete et al., 2005; Garnier et al., 2008; Nnafie et al., 2020; Thiébot et al., 2012) report migration rates 50% larger than the observed ones and growth times are also too large ($T_g \sim$1–2 days). In the only modelling study with $\theta > 5^\circ$ and $T_g < 1$ day (Klein & Schuttelaars, 2006), the migration speed is overpredicted by a factor of 6. The discrepancy between observed and modelled migration rates was also pointed out by Castelle et al. (2012). Including time-variable wave angles does not affect migration rates (Nnafie et al., 2020), but they decrease for larger grain sizes (Dong et al., 2015) or when including roller dynamics (Ribas et al., 2011). Finally, merging and splitting (as observed at Castelldefels) is clearly enhanced for variable offshore wave conditions (Castelle & Ruessink, 2011; Nnafie et al., 2020, 2021), due to the system adjusting to the new forcing.

6 | CONCLUSIONS

Over 7.5 years of daily time exposure images and propagated directional wave conditions (to 10 m depth) were used to study the dynamics of crescentic bars at Castelldefels beach (northwestern Mediterranean Sea). Formation and straightening moments of the crescentic bars were detected in detail, allowing an accurate assessment of the wave conditions during these moments. Throughout the study period, the beach was very dynamic and a total of 98 crescentic bar events were observed lasting 1389 days (48% of the time). Crescentic bar events occurred unevenly over the different years and their duration varied significantly during the study period (from days to months).

Crescentic bars were only observed when the sandbar was located at least 10 m from shore, indicating that crescentic bar formation depends strongly on the initial bathymetric configuration. The bar should not be located too far from shore either, as the low-energetic waves at the study site typically do not induce morphological changes at deeper water. As a result, the outer bar remained arrested during most of the study period. The sandbars experienced significant cross-shore movement during the study period and several moments of fast offshore migration occurred (up to 70 m in 1 day). Fast offshore migration was only observed during storms, but there were also many storms without major cross-shore movement. The observed fast offshore migration patterns are similar to episodic NOM, which has been described and observed in various previous studies.

A large variability (100–700 m) in crescentic bar wavelength was observed (due to splitting and merging) and wavelengths increased with bar–shoreline distance. The variation in amplitude (5–20 m) was limited. Compared to previous studies, the mean wavelengths and amplitudes (~200 m and ~9 m, respectively) are relatively small, which is probably due to the smaller mean wave energy at the study site. Alongshore migration speeds were mostly small (< 5 m/day), although larger values (up to 50 m/day) were observed during crescentic bar events with larger wavelengths and amplitudes. A clear relationship was found between the migration speed and S_{xy} (the alongshore component of the radiation stresses). Using S_{xy} values to compare modelled and observed migration speeds confirmed that existing models generally overpredict migration rates or underpredict growth times.

Average wave conditions at the study site were typically low–medium energetic waves (mean H_{m0} ~0.6 m) with a large variety in wave angle (up to 50°). Crescentic bar formation was mostly observed during low–medium energetic waves (average H_{m0} ~0.6 m) with both shore-normal and limited oblique angles of incidence ($\theta_{mean} \lesssim 20°$ at 10 m depth), including angles for which existing models predict straightening. Crescentic bar straightening could occur every few days and occurred both during medium and higher energetic waves (mean $H_{m0} = 0.73$ m). Wave angles were generally very oblique ($\theta_{mean} \gtrsim 15°$ at 10 m depth), which is a much larger threshold than obtained from model simulations. On the whole, the detailed wave conditions in the present study prove that existing crescentic bar modelling studies may be inaccurate during oblique waves, either underpredicting crescentic bar formation or overpredicting wavelengths and migration rates.

ACKNOWLEDGEMENTS

The maintenance of the video station has been a joint collaboration between the Coastal Morphodynamics Group (UPC) and the Institute of Marine Sciences (ICM-CSIC). We want to acknowledge the technical support from both institutions, in particular Oscar Chic (ICM-CSIC) and Toni Castillo (UPC). Furthermore, the authors would like to thank the city council of Castelldefels for allowing the installation of the video cameras and Pilar Gil from Puertos del Estado for providing the wave buoy data used in this study. The bathymetric data in Figure 1 were obtained from the European Marine Observation and Data Network (EMODnet, http://www.emodnet-bathymetry.eu/). Figures 5a and 6a use the scientific colour map roma (Crameri, 2019). This work has been funded by the Spanish government through the research projects CTM2015-66225-C2-1-P, CTM2015-66225-C2-2-P, RTI2018-093941-B-C32 and RTI2018-093941-B-C33 (MINECO/FEDER).

CONFLICT OF INTEREST

The authors declare that there are no conflicts of interest.

AUTHOR CONTRIBUTIONS

(a) conceptualization: RdS, FR, DC; (b) funding acquisition: FR, DC, GS, JG; (c) methodology: RdS, FR, DC; (d) investigation: RdS; (e) resources: RdS, FR, GS; (f) software: RdS, FR, GS; (g) supervision: FR, DC; (h) writing – initial draft: RdS; and (i) writing – reviewing and editing: RdS, FR, DC, GS, JG.

DATA AVAILABILITY STATEMENT

The research data from this study are available from the corresponding author upon reasonable request.

ORCID

Rinse L. de Swart https://orcid.org/0000-0001-6584-5184
Francesca Ribas https://orcid.org/0000-0003-4701-5982
Gonzalo Simarro https://orcid.org/0000-0002-6420-5975
Jorge Guillén https://orcid.org/0000-0001-7162-8135
Daniel Calvete https://orcid.org/0000-0002-5402-5137

REFERENCES

Aleman, N., Certain, R., Robin, N. & Barusseau, J.P. (2017) Morphodynamics of slightly oblique nearshore bars and their relationship with the cycle of net offshore migration. *Marine Geology*, 392(August), 41–52. https://doi.org/10.1016/j.margeo.2017.08.014.

Aleman, N., Robin, N., Certain, R., Anthony, E.J. & Barusseau, J.P. (2015) Longshore variability of beach states and bar types in a microtidal, storm-influenced, low-energy environment. *Geomorphology*, 241, 175–191. https://doi.org/10.1016/j.geomorph.2015.03.029.

Almar, R., Castelle, B., Ruessink, B.G., Sénéchal, N., Bonneton, P. & Marieu, V. (2010) Two- and three-dimensional double-sandbar system behaviour under intense wave forcing and a meso–macro tidal range. *Continental Shelf Research*, 30(7), 781–792. https://doi.org/10.1016/j.csr.2010.02.001.

Arifin, R.R. & Kennedy, A.B. (2011) The evolution of large scale crescentic bars on the northern Gulf of Mexico coast. *Marine Geology*, 285(1–4), 46–58. https://doi.org/10.1016/j.margeo.2011.04.003.

Armaroli, C. & Ciavola, P. (2011) Dynamics of a nearshore bar system in the northern Adriatic: A video-based morphological classification. *Geomorphology*, 126(1–2), 201–216. https://doi.org/10.1016/j.geomorph.2010.11.004.

Athanasiou, P., De Boer, W., Yoo, J., Ranasinghe, R. & Reniers, A. (2018) Analysing decadal-scale crescentic bar dynamics using satellite imagery: A case study at Anmok beach, South Korea. *Marine Geology*, 405(August), 1–11. https://doi.org/10.1016/j.margeo.2018.07.013.

Bolaños, R., Jorda, G., Cateura, J., Lopez, J., Puigefabregas, J., Gomez, J. & Espino, M. (2009) The XIOM: 20 years of a regional coastal observatory in the Spanish Catalan coast. *Journal of Marine Systems*, 77(3), 237–260. https://doi.org/10.1016/j.jmarsys.2007.12.018.

Bouvier, C., Balouin, Y. & Castelle, B. (2017) Video monitoring of sandbar-shoreline response to an offshore submerged structure at a microtidal beach. *Geomorphology*, 295(January), 297–305. https://doi.org/10.1016/j.geomorph.2017.07.017.

Calvete, D., Dodd, N., Falqués, A. & Van Leeuwen, S.M. (2005) Morphological development of rip channel systems: Normal and near-normal wave incidence. *Journal of Geophysical Research*, 110(C10), C10006. https://doi.org/10.1029/2004JC002803.

Calvete, D., Coco, G., Falqués, A. & Dodd, N. (2007) (Un)predictability in rip channel systems. *Geophysical Research Letters*, 34(5), L05605. https://doi.org/10.1029/2006GL028162.

Castelle, B. & Coco, G. (2012) The morphodynamics of rip channels on embayed beaches. *Continental Shelf Research*, 43, 10–23. https://doi.org/10.1016/j.csr.2012.04.010.

Castelle, B. & Coco, G. (2013) Surf zone flushing on embayed beaches. *Geophysical Research Letters*, 40(10), 2206–2210. https://doi.org/10.1002/grl.50485.

Castelle, B. & Ruessink, B.G. (2011) Modeling formation and subsequent nonlinear evolution of rip channels: Time-varying versus time-invariant wave forcing. *Journal of Geophysical Research*, 116(F4), F04008. https://doi.org/10.1029/2011JF001997.

Castelle, B., Bonneton, P., Dupuis, H. & Sénéchal, N. (2007) Double bar beach dynamics on the high-energy meso-macrotidal French Aquitanian coast: A review. *Marine Geology*, 245(1–4), 141–159. https://doi.org/10.1016/j.margeo.2007.06.001.

Castelle, B., Marieu, V., Coco, G., Bonneton, P., Bruneau, N. & Ruessink, B. G. (2012) On the impact of an offshore bathymetric anomaly on surf zone rip channels. *Journal of Geophysical Research: Earth Surface*, 117 (1), 1–20. https://doi.org/10.1029/2011JF002141.

Castelle, B., Marieu, V., Bujan, S., Splinter, K.D., Robinet, A., Sénéchal, N. & Ferreira, S. (2015) Impact of the winter 2013–2014 series of severe Western Europe storms on a double-barred sandy coast: Beach and dune erosion and megacusp embayments. *Geomorphology*, 238, 135–148. https://doi.org/10.1016/j.geomorph.2015.03.006.

Castelle, B., Scott, T., Brander, R.W. & McCarroll, R.J. (2016) Rip current types, circulation and hazard. *Earth-Science Reviews*, 163, 1–21. https://doi.org/10.1016/j.earscirev.2016.09.008.

Certain, R. (2002). Morphodynamique d'une côte sableuse microtidale à barres:le Golfe du Lion (Languedoc-Roussillon) (PhD thesis).

Contardo, S. & Symonds, G. (2015) Sandbar straightening under wind–sea and swell forcing. *Marine Geology*, 368, 25–41. https://doi.org/10.1016/j.margeo.2015.06.010.

Crameri, F. (2019). Scientific Colour Maps. https://doi.org/10.5281/zenodo.3596401#.YHcSSPmdYE.mendeley

Damgaard, J., Dodd, N., Hall, L. & Chesher, T. (2002) Morphodynamic modelling of rip channel growth. *Coastal Engineering*, 45(3–4), 199–221. https://doi.org/10.1061/40549%28276%2935.

De Swart, R.L., Ribas, F., Calvete, D., Kroon, A. & Orfila, A. (2020) Optimal estimations of directional wave conditions for nearshore field studies. *Continental Shelf Research*, 196, 104071. https://doi.org/10.1016/j.csr.2020.104071.

Deigaard, R., Drønen, N., Fredsøe, J., Jensen, J.H. & Jørgensen, M.P. (1999) A morphological stability analysis for a long straight barred coast. *Coastal Engineering*, 36(3), 171–195. https://doi.org/10.1016/S0378-3839(99)00005-8.

Dong, P., Chen, Y. & Chen, S. (2015) Sediment size effects on rip channel dynamics. *Coastal Engineering*, 99, 124–135. https://doi.org/10.1016/j.coastaleng.2015.03.001.

Gallagher, E.L., Elgar, S. & Guza, R.T. (1998) Observations of sand bar evolution on a natural beach. *Journal of Geophysical Research: Oceans*, 103(C2), 3203–3215. https://doi.org/10.1029/97JC02765.

Garnier, R., Calvete, D., Falqués, A. & Dodd, N. (2008) Modelling the formation and the long-term behavior of rip channel systems from the deformation of a longshore bar. *Journal of Geophysical Research: Oceans*, 113(7), 1–18. https://doi.org/10.1029/2007JC004632.

Garnier, R., Falqués, A., Calvete, D., Thiébot, J. & Ribas, F. (2013) A mechanism for sandbar straightening by oblique wave incidence. *Geophysical Research Letters*, 40(11), 2726–2730. https://doi.org/10.1002/grl.50464.

Gervais, M., Balouin, Y., Thiebot, J., Certain, R., Bélon, R., Pedreros, R. *et al.* (2011) Morphodynamic evolution of nearshore bars in response to winter storms (Lido de Séte, NW Mediterranean). *Journal of Coastal Research*, 64, 1855–1860.

Gervais, M., Balouin, Y. & Belon, R. (2012). Morphological response and coastal dynamics associated with major storm events along the Gulf of Lions Coastline, France. *Geomorphology*, 143-144, 69, 80, https://doi.org/10.1016/j.geomorph.2011.07.035

Gijsman, R., Ruessink, B.G., Visscher, J. & Schlurmann, T. (2021) Observations on decadal sandbar behaviour along a large-scale curved shoreline. *Earth Surface Processes and Landforms*, 46(2), 490–503. https://doi.org/10.1002/esp.5041.

Goldsmith, V., Bowman, D. & Kiley, K. (1982) Sequential stage development of crescentic bars: Hahoterim Beach, southeastern Mediterranean. *SEPM Journal of Sedimentary Research*, 52(1), 233–249.

Holman, R.A. & Stanley, J. (2007) The history and technical capabilities of Argus. *Coastal Engineering*, 54(6–7), 477–491. https://doi.org/10.1016/j.coastaleng.2007.01.003.

Holman, R.A., Symonds, G., Thornton, E.B. & Ranasinghe, R. (2006) Rip spacing and persistence on an embayed beach. *Journal of Geophysical Research*, 111(C1), C01006. https://doi.org/10.1029/2005JC002965.

Holthuijsen, L. H. (2007). *Waves in Oceanic and Coastal Waters*. Cambridge, UK: Cambridge University Press. http://ebooks.cambridge.org/ref/id/CBO9780511618536, https://doi.org/10.1017/CBO9780511618536.

Klein, M.D. & Schuttelaars, H.M. (2006) Morphodynamic evolution of double-barred beaches. *Journal of Geophysical Research*, 111(C6), C06017. https://doi.org/10.1029/2005JC003155.

Lippmann, T.C. & Holman, R.A. (1989) Quantification of sand bar morphology: A video technique based on wave dissipation. *Journal of Geophysical Research*, 94(C1), 995–1011. https://doi.org/10.1029/JC094iC01p00995.

Lippmann, T.C. & Holman, R.A. (1990) The spatial and temporal variability of sand bar morphology. *Journal of Geophysical Research*, 95(C7), 11575. https://doi.org/10.1029/JC095iC07p11575.

Melito, L., Parlagreco, L., Perugini, E., Postacchini, M., Devoti, S., Soldini, L. *et al.* (2020) Sandbar dynamics in microtidal environments: Migration patterns in unprotected and bounded beaches. *Coastal Engineering*, 161(October), 103768. https://doi.org/10.1016/j.coastaleng.2020.103768.

Nieto, M.A., Garau, B., Balle, S., Simarro, G., Zarruk, G.A., Ortiz, A. & Tintor'e, J., A´ lvarez-Ellacur'ıa, A., Go'mez-Pujol, L. & Orfila, A. (2010) An open source, low cost video-based coastal monitoring system. *Earth Surface Processes and Landforms*, 35(14), 1712–1719. https://doi.org/10.1002/esp.2025.

Nnafie, A., Van Andel, N. & De Swart, H.E. (2020) Modelling the impact of a time-varying wave angle on the nonlinear evolution of sand bars in the surf zone. *Earth Surface Processes and Landforms*, 45(11), 2603–2612. https://doi.org/10.1002/esp.4916.

Nnafie, A., Driessen, A.S., De Swart, H.E. & Price, T.D. (2021) Modelling the response of a double-barred sandy beach system to time-varying wave angles. *Earth Surface Processes and Landforms*, 46(7), 1393–1409. https://doi.org/10.1002/esp.5107.

Ojeda, E. & Guill'en, J. (2008) Shoreline dynamics and beach rotation of artificial embayed beaches. *Marine Geology*, 253(1–2), 51–62. https://doi.org/10.1016/j.margeo.2008.03.010.

Ojeda, E. & Guill'en, J. & Ribas, F. (2011) Dynamics of single-barred embayed beaches. *Marine Geology*, 280(1–4), 76–90. https://doi.org/10.1016/j.margeo.2010.12.002.

Orzech, M.D., Thornton, E.B., MacMahan, J.H., O'Reilly, W.C. & Stanton, T.P. (2010) Alongshore rip channel migration and sediment transport. *Marine Geology*, 271(3-4), 278–291. https://doi.org/10.1016/j.margeo.2010.02.022.

Orzech, M.D., Reniers, A.J.H.M., Thornton, E.B. & MacMahan, J.H. (2011) Megacusps on rip channel bathymetry: Observations and modeling. *Coastal Engineering*, 58(9), 890–907. https://doi.org/10.1016/j.coastaleng.2011.05.001.

Pape, L. (2008) *BLIM Toolbox Manual: IMAU Report R08–02 (November)*.

Parlagreco, L., Melito, L., Devoti, S., Perugini, E., Soldini, L., Zitti, G. & Brocchini, M. (2019) Monitoring for coastal resilience: Preliminary data from five Italian sandy beaches. *Sensors*, 19(8), 1854. https://doi.org/10.3390/s19081854.

Price, T.D. & Ruessink, B.G. (2011) State dynamics of a double sandbar system. *Continental Shelf Research*, 31(6), 659–674. https://doi.org/10.1016/j.csr.2010.12.018.

Price, T.D., Castelle, B., Ranasinghe, R. & Ruessink, B.G. (2013) Coupled sandbar patterns and obliquely incident waves. *Journal of Geophysical Research: Earth Surface*, 118(3), 1677–1692. https://doi.org/10.1002/jgrf.20103.

Puertos del Estado. (1994). Maritime Works Recommendations. ROM 0.3–91 Waves Annex 1: Wave Climate on the Spanish coast: Ministerio de Obras Publicas y Transporte, Centro de Publicaciones de Secretar'ıa General T'ecnica.

Ranasinghe, R., Symonds, G., Black, K. & Holman, R. (2004) Morphodynamics of intermediate beaches: A video imaging and

numerical modelling study. *Coastal Engineering*, 51(7), 629–655. https://doi.org/10.1016/j.coastaleng.2004.07.018.

Reniers, A.J.H.M., Roelvink, J.A. & Thornton, E.B. (2004) Morphodynamic modeling of an embayed beach under wave group forcing. *Journal of Geophysical Research*, 109(C1), C01030. https://doi.org/10.1029/2002JC001586.

Ribas, F., Ojeda, E., Price, T.D. & Guill'en, J. (2010) Assessing the suitability of video imaging for studying the dynamics of nearshore sandbars in tideless beaches. *IEEE Transactions on Geoscience and Remote Sensing*, 48(6), 2482–2497. https://doi.org/10.1109/TGRS.2009.2039576.

Ribas, F., De Swart, H.E., Calvete, D. & Falqu'es, A. (2011) Modeling waves, currents and sandbars on natural beaches: The effect of surface rollers. *Journal of Marine Systems*, 88(1), 90–101. https://doi.org/10.1016/j.jmarsys.2011.02.016.

Ribas, F., Falqués, A., De Swart, H.E., Dodd, N., Garnier, R. & Calvete, D. (2015) Understanding coastal morphodynamic patterns from depth-averaged sediment concentration. *Reviews of Geophysics*, 53(2), 362–410. https://doi.org/10.1002/2014RG000457.

Ribas, F., Falqués, A. & Garnier, R. (2017). *Nearshore sand bars on Western Mediterranean beaches, Atlas of bedforms in the Western Mediterranean*. Cham: Springer (pp. 81–88). https://doi.org/10.1007/978-3-319-33940-5 14.

Ribas, F., Simarro, G., Arriaga, J. & Luque, P. (2020) Automatic shoreline detection from video images by combining information from different methods. *Remote Sensing*, 12(22), 3717. https://doi.org/10.3390/rs12223717.

Ruessink, B.G. & Kroon, A. (1994) The behaviour of a multiple bar system in the nearshore zone of Terschelling, the Netherlands: 1965–1993. *Marine Geology*, 121(3–4), 187–197. https://doi.org/10.1016/0025-3227(94)90030-2.

Ruessink, B.G., Van Enckevort, I.M.J., Kingston, K.S. & Davidson, M.A. (2000) Analysis of observed two- and three-dimensional nearshore bar behaviour. *Marine Geology*, 169(1–2), 161–183. https://doi.org/10.1016/S0025-3227(00)00060-8.

Ruessink, B.G., Pape, L. & Turner, I.L. (2009) Daily to interannual cross-shore sandbar migration: Observations from a multiple sandbar system. *Continental Shelf Research*, 29(14), 1663–1677. https://doi.org/10.1016/j.csr.2009.05.011.

Rutten, J., Ruessink, B.G. & Price, T.D. (2018) Observations on sandbar behaviour along a man-made curved coast. *Earth Surface Processes and Landforms*, 43(1), 134–149. https://doi.org/10.1002/esp.4158.

Rutten, J., Dubarbier, B., Price, T.D., Ruessink, B.G. & Castelle, B. (2019) Alongshore variability in crescentic sandbar patterns at a strongly curved coast. *Journal of Geophysical Research: Earth Surface*, 124(12), 2877–2898. https://doi.org/10.1029/2019JF005041.

Sánchez-Arcilla, A., González-Marco, D. & Bolaños, R. (2008) A review of wave climate and prediction along the Spanish Mediterranean coast. *Natural Hazards and Earth System Science*, 8(6), 1217–1228. https://doi.org/10.5194/nhess-8-1217-2008.

Scott, T., Masselink, G., Austin, M.J. & Russell, P. (2014) Controls on macrotidal rip current circulation and hazard. *Geomorphology*, 214, 198–215. https://doi.org/10.1016/j.geomorph.2014.02.005.

Shand, R.D., Bailey, D.G. & Shepherd, M.J. (1999) An inter-site comparison of net offshore bar migration characteristics and environmental conditions. *Journal of Coastal Research*, 15(3), 750–765.

Short, A.D. & Aagaard, T. (1993) Single and multi-bar beach change models. *Journal of Coastal Research*, 1993(Special issue 15), 141–157.

Simarro, G., Bryan, K.R., Guedes, R.M.C., Sancho, A., Guillen, J. & Coco, G. (2015) On the use of variance images for runup and shoreline detection. *Coastal Engineering*, 99, 136–147. https://doi.org/10.1016/j.coastaleng.2015.03.002.

Simarro, G., Ribas, F., Álvarez, A., Guillén, J., Chic, O. & Orfila, A. (2017) ULISES: An open source code for extrinsic calibrations and planview generations in coastal video monitoring systems. *Journal of Coastal Research*, 335, 1217–1227.

Smit, M.W.J., Reniers, A.J.H.M., Ruessink, B.G. & Roelvink, J.A. (2008) The morphological response of a nearshore double sandbar system to constant wave forcing. *Coastal Engineering*, 55(10), 761–770. https://doi.org/10.1016/j.coastaleng.2008.02.010.

Smit, M.W.J., Reniers, A.J.H.M. & Stive, M.J.F. (2012) Role of morphological variability in the evolution of nearshore sandbars. *Coastal Engineering*, 69, 19–28. https://doi.org/10.1016/j.coastaleng.2012.05.005.

Thiébot, J., Idier, D., Garnier, R., Falqués, A. & Ruessink, B.G. (2012) The influence of wave direction on the morphological response of a double sandbar system. *Continental Shelf Research*, 32, 71–85. https://doi.org/10.1016/j.csr.2011.10.014.

Thornton, E.B., MacMahan, J. & Sallenger, A.H. (2007) Rip currents, megacusps, and eroding dunes. *Marine Geology*, 240(1–4), 151–167. https://doi.org/10.1016/j.margeo.2007.02.018.

Tiessen, M.C.H., Van Leeuwen, S.M., Calvete, D. & Dodd, N. (2010) A field test of a linear stability model for crescentic bars. *Coastal Engineering*, 57(1), 41–51. https://doi.org/10.1016/j.coastaleng.2009.09.002.

Tiessen, M.C.H., Dodd, N. & Garnier, R. (2011) Development of crescentic bars for a periodically perturbed initial bathymetry. *Journal of Geophysical Research: Earth Surface*, 116(4), 1–24. https://doi.org/10.1029/2011JF002069.

Van Enckevort, I.M.J. & Ruessink, B.G. (2001) Effect of hydrodynamics and bathymetry on video estimates of nearshore sandbar position. *Journal of Geophysical Research: Oceans*, 106(C8), 16969–16979. https://doi.org/10.1029/1999JC000167.

Van Enckevort, I.M.J., Ruessink, B.G., Coco, G., Suzuki, K., Turner, I.L., Plant, N.G. & Holman, R.A. (2004) Observations of nearshore crescentic sandbars. *Journal of Geophysical Research*, 109(C6), C06028. https://doi.org/10.1029/2003JC002214.

Van de Lageweg, W.I., Bryan, K.R., Coco, G. & Ruessink, B.G. (2013) Observations of shoreline–sandbar coupling on an embayed beach. *Marine Geology*, 344, 101–114. https://doi.org/10.1016/j.margeo.2013.07.018.

Wright, L.D. & Short, A.D. (1984) Morphodynamic variability of surf zones and beaches: A synthesis. *Marine Geology*, 56(1–4), 93–118. https://doi.org/10.1016/0025-3227(84)90008-2.

SUPPORTING INFORMATION

Additional supporting information may be found in the online version of the article at the publisher's website.

How to cite this article: de Swart, R.L., Ribas, F., Simarro, G., Guillén, J. & Calvete, D. (2021) The role of bathymetry and directional wave conditions on observed crescentic bar dynamics. *Earth Surface Processes and Landforms*, 1–19. Available from: https://doi.org/10.1002/esp.5233